

**UNIVERSIDADE DE SÃO PAULO  
INSTITUTO DE FÍSICA DE SÃO CARLOS**

**Vitor Diorio Lordello**

**Cosmic ray  $^2\text{H}/^1\text{H}$  flux ratio measurement with the  
AMS-02 experiment.**

**São Carlos**

**2017**



**Vitor Diorio Lordello**

**Cosmic ray  $^2\text{H}/^1\text{H}$  flux ratio measurement with the  
AMS-02 experiment.**

Dissertation presented to the Graduate Program in Physics at the Instituto de Física de São Carlos, Universidade de São Paulo, to obtain the degree of Master in Science.

Concentration area: Applied Physics

Advisor: Prof<sup>ca</sup>. Dra. Manuela Vecchi

**Corrected version  
(Original version available on the Program Unit)**

**São Carlos  
2017**

I AUTHORIZE THE REPRODUCTION AND DISSEMINATION OF TOTAL OR PARTIAL COPIES OF THIS DOCUMENT, BY CONVENCIONAL OR ELECTRONIC MEDIA FOR STUDY OR RESEARCH PURPOSE, SINCE IT IS REFERENCED.

Cataloguing data revised by the Library and Information Service  
of the IFSC, with information provided by the author

Lordello, Vitor Diorio

Cosmic ray  $2\text{H}/1\text{H}$  flux ratio measurement with the  
AMS-02 experiment / Vitor Diorio Lordello; advisor  
Manuela Vecchi - revised version -- São Carlos 2017.  
68 p.

Dissertation (Master's degree - Graduate Program  
in Applied Physics) -- Instituto de Física de São  
Carlos, Universidade de São Paulo - Brasil , 2017.

1. Astroparticle physics. 2. AMS-02. 3. Cosmic-  
ray flux. 4. Cosmic-ray deuterium measurement. 5.  
Cosmic-ray isotope separation. I. Vecchi, Manuela,  
advisor. II. Title.

## **ACKNOWLEDGEMENTS**

I would like to thank my advisor, Prof. Manuela Vecchi for her support, enthusiasm and patience, as well as to CNPq and IFSC for supporting my research.



## ABSTRACT

LORDELLO, V. D. **Cosmic ray  $^2\text{H}/^1\text{H}$  flux ratio measurement with the AMS-02 experiment.** 2017. 68p. Dissertação (Mestrado em Ciências) - Instituto de Física de São Carlos, Universidade de São Paulo, São Carlos, 2017.

The Alpha Magnetic Spectrometer (AMS-02) is a cosmic ray detector operating aboard the International Space Station (ISS) since May 2011. The identification of cosmic ray deuterium and hydrogen particles is the main goal of this work. Using the data collected by the AMS-02 experiment between May 2011 and May 2014 we provide the measurement of the  $^2\text{H}$  to the  $^1\text{H}$  ratio between 0.7 and 7  $\text{GeV}/n$ .

Cosmic rays are mainly composed of hydrogen nuclei. No significant amount of deuterium nuclei is expected to be released from galactic sources since they are destroyed rather than formed in thermonuclear reactions inside stars. As a consequence of their production history, they are part of a class of secondary stable nuclei that provide information on the propagation of cosmic rays in the galaxy. Despite their relevance for propagation studies, very few measurements of deuterium exist above 1  $\text{GeV}/n$ , due to the poor isotopic separation capacity of previous experiments. For this reason, the deuterium to hydrogen flux ratio is a very important measurement to be carried out using the data collected by the AMS-02 experiment. The mass and the isotopic composition of cosmic-rays nuclei can be measured by the AMS-02 experiment using measurements of the momentum (provided by the tracker) and velocity of the particles (provided by the Time-of-Flight and the RICH). This analysis is one of the first to be focused on hydrogen isotopic composition with AMS-02 data, and our results are in fair agreement with a similar and independent analysis that has been carried out within the Collaboration.

**Keywords:** Astroparticle physics. AMS-02. Cosmic-ray flux. Cosmic-ray deuterium measurement. Cosmic-ray isotope separation.



## RESUMO

LORDELLO, V. D. **Medição da razão  $^2\text{H}/^1\text{H}$  de fluxo em raios cósmicos com o experimento AMS-02.** 2017. 68p. Dissertação (Mestrado em Ciências) - Instituto de Física de São Carlos, Universidade de São Paulo, São Carlos, 2017.

O Espectômetro Magnético Alpha (AMS-02) é um detetor de raios cósmicos operando na Estação Espacial Internacional (ISS) desde maio de 2011. O principal objetivo deste trabalho é a identificação de deutério e hidrogênio nos raios cósmicos. Usando dados coletados pelo experimento AMS-02 entre maio de 2011 e maio de 2014 foi medida a razão entre os fluxos de  $^2\text{H}$  e  $^1\text{H}$  entre 0.7 e 7  $\text{GeV}/n$ .

Raios cósmicos são compostos, principalmente, por núcleos de hidrogênio. Não é esperado que fontes galácticas de raios cósmicos liberem uma quantidade significativa de núcleos de deutério, já que eles são destruídos, em vez de formados, nas reações termonucleares no interior de estrelas. Assim, eles fazem parte de uma classe de partículas secundárias estáveis que fornecem informações acerca da propagação de raios cósmicos na galáxia. Apesar da relevância para o estudo da propagação de raios cósmicos, poucas medidas da sua quantidade acima de 1  $\text{GeV}/n$  existem, devido à baixa capacidade de separação de isótopos de prévios experimentos. Por isso a razão entre os fluxos de deutério e hidrogênio é uma importante medida a ser feita com os dados do AMS-02. A massa, e portanto a composição isotópica dos raios cósmicos, pode ser medida pelo AMS-02 a partir das medições de momento (realizada pelo tracker) e velocidade (realizadas pelo ToF e RICH). Essa análise é uma das primeiras a focar na composição isotópica do hidrogênio com dados do AMS-02, e os resultados estão razoavelmente em acordo com análises independentes semelhantes realizadas na colaboração AMS.

**Palavras-chave:** Física de astropartículas. AMS-02. Fluxo de raios cósmicos. Medida de deutério nos raios cósmicos. Separação de isótopos nos raios cósmicos.



## CONTENTS

<b>1</b>	<b>COSMIC RAYS</b> . . . . .	<b>11</b>
<b>1.1</b>	<b>Introduction</b> . . . . .	<b>11</b>
<b>1.2</b>	<b>The flux</b> . . . . .	<b>11</b>
<b>1.3</b>	<b>Composition</b> . . . . .	<b>14</b>
<b>1.4</b>	<b>Origin and propagation of galactic CRs.</b> . . . . .	<b>15</b>
1.4.1	Acceleration in SNRs . . . . .	15
1.4.2	Galactic Diffusion . . . . .	16
1.4.3	Cosmic Rays in the Heliosphere . . . . .	18
1.4.4	Cosmic Rays in the Magnetosphere . . . . .	19
<b>1.5</b>	<b>Deuterium Phenomenogy</b> . . . . .	<b>20</b>
<b>2</b>	<b>THE ALPHA MAGNETIC SPECTROMETER</b> . . . . .	<b>25</b>
<b>2.1</b>	<b>Transition Radiation Detector</b> . . . . .	<b>26</b>
<b>2.2</b>	<b>Time Of Flight</b> . . . . .	<b>28</b>
<b>2.3</b>	<b>Tracker</b> . . . . .	<b>29</b>
<b>2.4</b>	<b>Ring Imaging Detector</b> . . . . .	<b>31</b>
<b>2.5</b>	<b>Anti-Coincidence Counter</b> . . . . .	<b>33</b>
<b>2.6</b>	<b>The Electromagnetic Calorimeter</b> . . . . .	<b>33</b>
<b>3</b>	<b>MEASUREMENT OF COSMIC RAY PROPERTIES WITH AMS-02</b>	<b>37</b>
<b>3.1</b>	<b>Charge Measurement</b> . . . . .	<b>37</b>
3.1.1	Tracker . . . . .	37
3.1.2	Time of flight . . . . .	39
<b>3.2</b>	<b>Momentum Measurement</b> . . . . .	<b>41</b>
<b>3.3</b>	<b>Mass measurement</b> . . . . .	<b>44</b>
<b>4</b>	<b>MEASUREMENT OF <math>^2\text{H}</math> AND <math>^1\text{H}</math> WITH THE AMS-02 DETECTOR</b>	<b>47</b>
<b>4.1</b>	<b>Event counting Method</b> . . . . .	<b>55</b>
<b>4.2</b>	<b>Flux ratio measurement</b> . . . . .	<b>56</b>
<b>4.3</b>	<b>Final Results</b> . . . . .	<b>58</b>
<b>5</b>	<b>CONCLUSIONS AND PERSPECTIVES</b> . . . . .	<b>63</b>
	<b>REFERENCES</b> . . . . .	<b>65</b>



# 1 COSMIC RAYS

## 1.1 Introduction

Cosmic Rays (CRs) are high-energy particles mainly produced outside the solar system.<sup>1</sup> CRs are largely composed of protons ( $\sim 90\%$ ) and helium nuclei ( $\sim 9\%$ ), while the remaining  $\sim 1\%$  is composed of electrons, fully ionized nuclei and traces of anti-matter. The chemical and isotopic composition, as well as the energy spectrum of CRs, carry important information both on their origin (sources and acceleration mechanisms) and on the properties of the interstellar medium which they traverse during their journey to Earth (magnetic fields, interstellar matter density, diffusion mechanisms). Therefore the combined study of cosmic rays of different nature and energies (multi-messenger astrophysics) and accurate measurements of the CR properties can contribute to a deeper understanding of their astrophysical source characteristics, to a better modeling of CR propagation in the galaxy and can also unveil the presence of new particles produced in earlier stages of the Universe.

Deuterium nuclei, or deuterons, are present in CRs as a result of nuclear interactions, mainly of  $^1\text{H}$  and  $^4\text{He}$  nuclei with the interstellar medium. As a consequence, their flux measurement in the GeV to TeV energy range provides information on their propagation in the galaxy. Despite its scientific relevance, few experimental data exists in this energy range, due to the difficulties of such measurements.

The identification of CR deuterium and hydrogen particles in the GeV energy region is the main goal of this work. Using the data collected by the AMS-02 experiment between May 2011 and May 2014 we provide the measurement of the  $^2\text{H}$  to the  $^1\text{H}$  ratio between 0.7 and 7  $\text{GeV}/n$  of kinetic energy per nucleon.

The first chapter of this work provides an introduction to CR origin, propagation, and composition, together with a review of existing deuterium measurements. A description of the AMS-02 detector is given in the second chapter. The third chapter describes the measurements of the CR properties with AMS-02, namely charge, momentum and mass. Finally, chapter four describes the  $^2\text{H}$  and  $^1\text{H}$  flux measurements as a function of the kinetic energy per nucleon, and chapter five presents the results and conclusions of the present work.

## 1.2 The flux

The all-particle CR flux, i.e. the number of particles detected per unit detection area, per unit detection time, per energy interval, per unit of detection solid angle, is shown in figure 1. This plot is a compilation of recent available measurements.

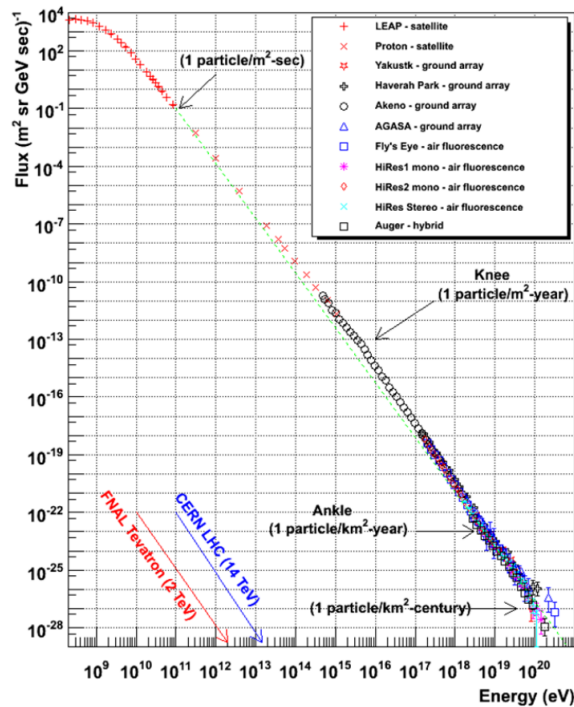


Figure 1 – Overall differential energy spectra of cosmic rays from various experiments. Interesting features in the spectrum are indicated like the *knee* at  $10^{15}$  eV and the *ankle* at  $10^{18}$  eV. The frequencies of arrival of particles of different energies are indicated, as well as the center of mass energies attainable in different accelerator experiments.

Source: [LONGAIR<sup>1</sup>](#)

We can see that the CR flux is a strongly decreasing function of energy: at first sight, the flux above a few *GeV* appears as a featureless power law, with spectral index around 2.7, extending over some 12 orders of magnitude in energy and 33 orders of magnitude in flux. Interesting features appear more visibly if we multiply the flux by some power of the energy, typically between 2 and 3. Figure 2 shows the all-particle flux multiplied by the energy to the power 2.6, and a few features appear more clearly: a first transition in the spectral index, dubbed *knee*, is characterized by a steepening of the spectrum at around  $10^{15}$  eV, then a *second knee* appears around  $10^{17}$  eV and an *ankle* around  $10^{18}$  eV. These features are all related to the origin and propagation history of CRs in the galaxy and beyond.

In the conventional model for CR production,<sup>1</sup> particles with energies lower than  $10^{15}$  eV are believed to be accelerated by galactic sources such as supernova remnants (SNRs). In this picture, particles are scattered across the shock fronts of the supernova, gaining energy at each crossing by the first order Fermi process. This acceleration model is strongly supported by recent observations of  $\gamma$ -ray emission from SNR<sup>3,4</sup> revealing the presence of energetic particles near these objects.

At energies  $\sim 10^{15}$  eV the CR spectrum has a steepening, the *knee*, characterized

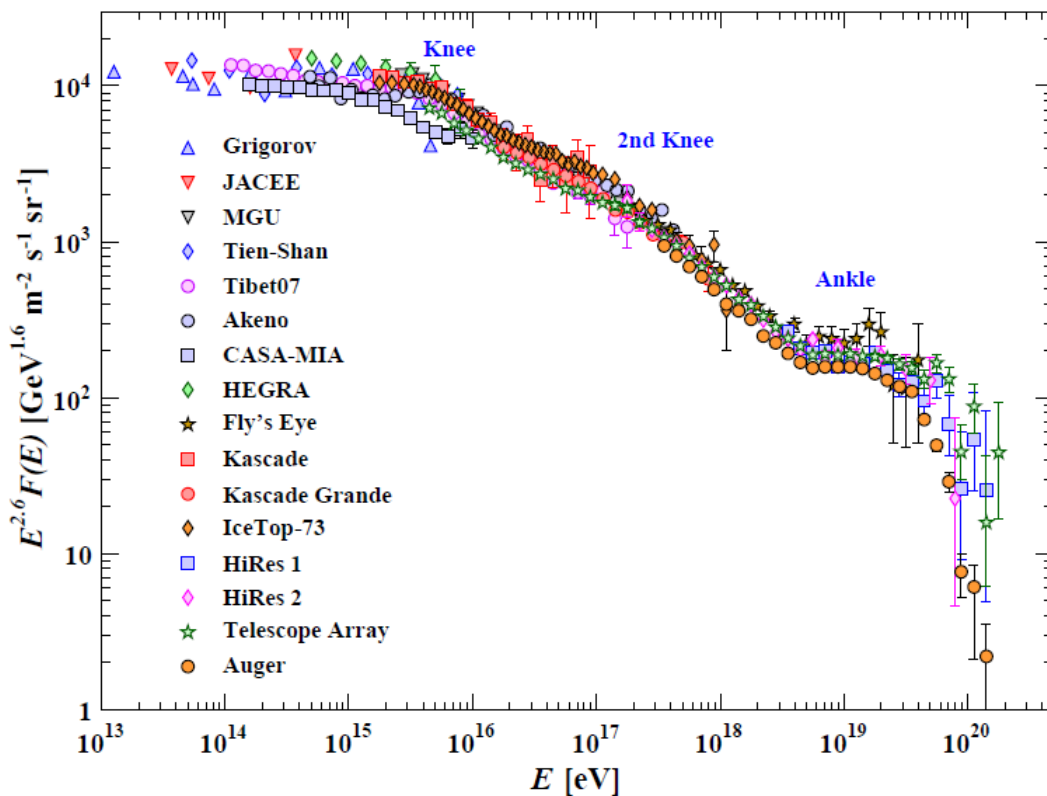


Figure 2 – The all-particle flux rescaled by  $E^{2.6}$ , as a function of energy.

Source: [PATRIGNANI<sup>2</sup>](#)

by a sudden variation of the all-species spectral index from 2.7 to 3.1. The knee is thought to reflect the fact that most cosmic accelerators in the galaxy have reached their maximum energy. Some types of expanding supernova remnants,<sup>1</sup> for example, are estimated not to be able to accelerate protons above energies in the range of  $10^{15}$  eV. A second knee is observed in the spectrum around  $E \sim 10^{17}$  eV with evidence that this structure is accompanied a composition transition<sup>5</sup> to heavy primaries. This could be due to the decreasing efficiency in the galactic magnetic confinement for more energetic particles, leading to a CR leakage from the galaxy.

The structure at  $E \sim 10^{18}$  eV, called the ankle, is likely to be the result of a higher energy population of extragalactic particles beginning to dominate over the lower energy galactic population. Another possibility is that it is due to energy loss related to  $e^+ + e^-$  pair production of extragalactic protons in the interactions on the 2.7 K Cosmic Microwave Background radiation (CMB).<sup>6</sup> This structure has been cited as a robust signature of both the protonic and extragalactic nature of the highest energy cosmic rays.<sup>7</sup> The energy dependence of the composition from the knee through the ankle is useful in discriminating between these two viewpoints, since a heavy composition above  $10^{18}$  eV is inconsistent with the formation of the ankle by pair production losses on the CMB.

The nature and origin of Ultra-High-Energy Cosmic Rays (UHECRs) with energies higher

than  $10^{19}$  eV are, as of today, under debate.<sup>8</sup> Not only the cosmological sources and acceleration mechanisms that could produce such energetic particles are still unclear, but even their possibility to reach us is highly suppressed due to their inelastic interaction ( $\pi$  production) with the CMB, creating a drastic flux reduction known as the Greisen-Zatsepin-Kuzmin (GZK) cut-off limit.<sup>9</sup> The flux suppression has been confirmed by the Auger observatory<sup>10</sup> as well as by the Telescope Array<sup>11</sup> experiments with high statistical significance, though its explanation is still being debated.

### 1.3 Composition

Cosmic rays include essentially all the elements in the periodic table: about 90% of the nuclei are hydrogen (protons), 9% helium, and about 1% are heavier elements nuclei.<sup>12</sup> figure 3 shows the relative abundance of these elements as they are found in both CRs and the solar system, considered to have a composition typical of CR sources. Heavy elements such as carbon, nitrogen, oxygen, magnesium, silicon and iron are present in CRs at about the same relative abundances as in the solar system, but there are important differences in elemental and isotopic composition that provide information on the origin and history of galactic cosmic rays.

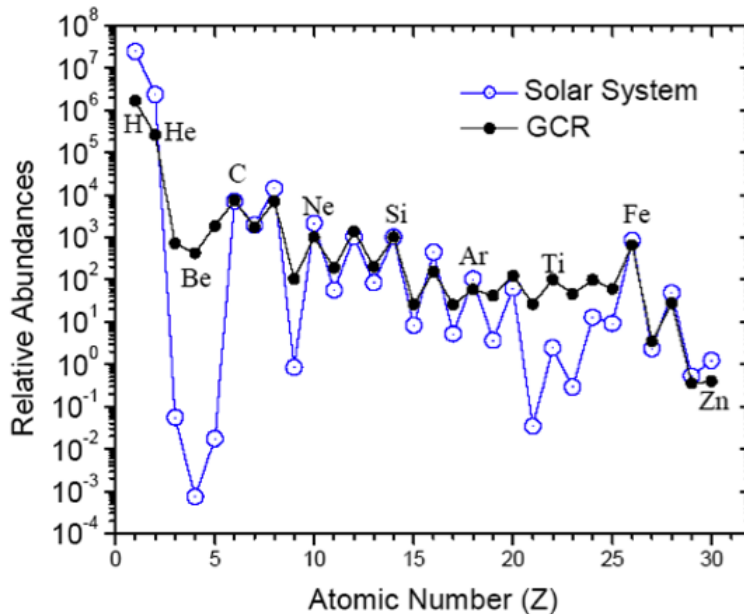


Figure 3 – Composition of galactic CRs and of the solar system. Both are normalized to the abundance of Si =  $10^3$ , and the energy range is a few hundreds MeV/nucleon.

Source: SIMPSON<sup>12</sup>

A significant overabundance of the rare elements such as lithium, beryllium and boron is observed in galactic CRs with respect to the solar system. These nuclei are thought to be produced when heavier cosmic rays such as carbon, nitrogen, and oxygen undergo

spallation processes as a consequence of their propagation in the interstellar medium. These differences show that the nucleosynthesis of cosmic rays and solar system material have differed.

An alternating pattern of higher and lower fluxes for adjacent species can be seen after the carbon nuclei, in both solar system and CR abundance. This is because odd atomic number nuclei are weakly bounded and can be destroyed in the stellar thermonuclear reactions, while even nuclides are much more stable and consequently more abundant. The spallation of nuclei with even atomic number can also contribute to the higher abundance of the odd nuclei observed in CRs as compared to that in the solar system.

In the following we will use the following definitions: “primary” cosmic rays are the particles accelerated at astrophysical sources, while “secondaries” are the particles produced in interactions of the primaries with interstellar gas. Thus electrons, protons and helium, as well as carbon, oxygen and iron are primaries. Nuclei such as lithium, beryllium, and boron, which are not abundant end-products of stellar nucleosynthesis, are secondaries. Antiprotons and positrons are also in large part secondaries, though whether a significant fraction of these particles may be of primary origin is a question of current interest.<sup>13,14</sup> Up to now there is no evidence for the existence of heavier anti-nuclei (in particular anti-deuterium and anti-helium) in cosmic rays,<sup>15</sup> which could indicate the existence of anti-matter domains in the universe.<sup>16</sup>

## 1.4 Origin and propagation of galactic CRs.

As discussed, primary CRs are produced and accelerated in astrophysical sources. Typically these particles are accelerated by shock waves and confined by galactic magnetic fields during a journey of several *Myr* before their arrival to Earth.<sup>17</sup> On their way to the solar system, the CR composition is modified as they propagate through the interstellar medium (ISM) due to spallation processes, producing secondary CRs. As they arrive in the solar system and come to Earth, the spectrum is further modified by solar winds and magnetic fields. These processes are discussed below.

### 1.4.1 Acceleration in SNRs

The diffusive shock acceleration (DSA) theory<sup>18</sup> is able to explain the power-law spectrum ( $\text{Flux} \propto E^{-\gamma}$ ) observed in galactic CRs above  $\sim 10 \text{ GeV}/n$  of energy per nucleon. It is believed to apply to a wide range of space environments, and is based on the first order Fermi acceleration theory, which leads to an efficient energy gain through individual head-on collisions of accelerated particles with shock waves. It has been proposed as the explanation for the acceleration of galactic CRs at shock-fronts where young supernova remnants interact with the interstellar medium and has been validated by recent observational and theoretical developments. The observational development includes

$MeV$  to  $TeV$  photon data from young supernovae and the theoretical development is the suggestion that CRs can cause the magnetic field to be amplified by a very large factor in association with these shocks.<sup>19</sup>

In this picture, particles bounce back and forth across a shock wave, as illustrated in figure 4. As the shock travels, it creates two regions, the upstream and downstream regions, labeled 1 and 2, which have different fluid velocity. Consider a particle on side 1 about to cross the shock and enter side 2. The scattering centers on side 2 are convected along with the plasma. Once the particle crosses the shock, it is scattered and gains energy due to the oncoming motion of the scatterers. After being scattered various times on side 2, the particle can diffuse back to the shock and cross back onto side 1. On doing so, it sees the scattering centers on side 1 approaching it head on and again it gains energy on being scattered back on side 1. As this happens multiple times, the pressure associated with the fast particles becomes comparable to the thermal pressure of the plasma, and the structure of the shock is modified by this pressure. Such effects provide a constraint on DSA energy transfer.

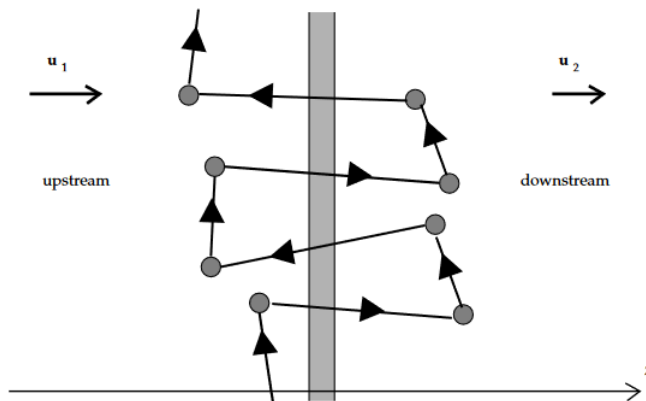


Figure 4 – Diffusive shock acceleration is illustrated: the shaded vertical region is the shock, the circular blobs denote idealized scattering centers, and the solid line with arrows denotes the path of an idealized fast particle.

Source: MELROSE<sup>19</sup>

For strong shocks, the spectral index is close to the value 2 and it is independent of the SNR properties such as ambient density, magnetic field intensity or turbulence. Therefore, this mechanism provides an excellent physical reason why power-law energy spectra with a unique spectral index may occur in different astrophysical environments.

#### 1.4.2 Galactic Diffusion

Galactic CRs are thought to propagate mainly by diffusion due to scattering on random or turbulent magnetic fields.<sup>20</sup> The spatial diffusion coefficient,  $D_{xx}$ , depends on

particle momentum  $p$ . The particle spectra are modified along the way by energy losses and by diffusive re-acceleration. Energy losses include a large variety of processes, such as ionization and Coulomb interactions with interstellar gas (dominant for low-energy CR nuclei) and hadronic interactions like pion production (dominant for high-energy nuclei). Lepton energy losses are more severe as those of nuclei, and they are due to synchrotron radiation, bremsstrahlung, and inverse-Compton interactions, as well as ionization and Coulomb losses. Primary CRs also undergo nuclear interactions with the interstellar gas, producing secondary nuclei by spallation. CR dynamics in the galaxy is therefore generally described by a differential equation that includes acceleration, loss, and transport terms.<sup>21</sup> CR sources are concentrated in the Galactic plane, and the particles undergo large numbers of scatterings before finally escaping into intergalactic space. The escape is an essential, but little understood, part of their history and is usually treated simply by setting the CR density to zero at some boundary a few kiloparsecs above the Galactic plane. The region occupied by CRs is often referred to as the CR halo, and similar halos are observed in the radio synchrotron emission from external galaxies viewed edge-on.

The simplest description of this phase, the leaky-box model, assumes a galaxy with uniform density from which cosmic rays escape or leak out with an energy-dependent probability per unit time. More realistic models account for the actual structure of the Galaxy, incorporating both a high-density central disk and a low-density halo and transport mechanisms within the Local Bubble. In this model CRs might lose or gain energy, their initial spectra and composition can change, they can produce secondary particles and  $\gamma$ -rays. All these effects, enter explicitly in the current diffusion models where a steady-state equilibrium of the CR distribution in the galaxy is obtained taking into account galactic wind (convection), diffusive re-acceleration in the ISM, energy losses, nuclear fragmentation and decay, as described by the transport equation:

$$\frac{\partial \psi}{\partial t} = q(\vec{r}, p) + \vec{\nabla} \cdot (D_{xx} \vec{\nabla} \psi - \vec{V} \psi) + \frac{\partial}{\partial p} p^2 D_{pp} \frac{\partial}{\partial p} \frac{1}{p^2} \psi - \frac{\partial}{\partial p} \left[ \dot{p} \psi - \frac{p}{3} (\vec{\nabla} \cdot \vec{V}) \psi \right] - \frac{1}{\tau_f} - \frac{1}{\tau_r} \quad (1.1)$$

Where:

- $\psi(\vec{r}, p, t)$  is the density per unit of total particle momentum, with  $\psi(p)dp = 4\pi p^2 f(\vec{p})d\vec{p}$  in terms of the phase-space density  $f(\vec{p})$ ;
- $q(\vec{r}, p)$  is the source term;
- $D_{xx}$  is the diffusion coefficient;
- $D_{pp}$  is the re-acceleration, described as diffusion in momentum space;
- $\vec{V}$  is the convection velocity;

- $\dot{p}$  is the momentum loss rate described for nucleons by ionization and Coulomb interactions, and for electrons by ionization, Coulomb interactions, bremsstrahlung, inverse Compton, and synchrotron radiation;
- $\tau_f$  is the timescale for fragmentation;
- $\tau_r$  is the timescale for the radioactive decay.

Secondary stable elements as  $^2\text{H}$ ,  $^3\text{He}$ , Li, Be, B as well as the sub-iron elements (Sc, Ti and V), are almost entirely originated in the spallation of primary nuclei, and their abundances depend on the original primary composition and on the galactic CR propagation mechanism. In the context of the propagation models, secondary-to-primary CR flux ratios, such as Boron-to-Carbon or  $^3\text{He}/^4\text{He}$  flux ratios, are used to study the propagation of CRs in the galaxy.<sup>22-23</sup> Besides secondary-to-primary flux ratios, many different types of CRs with particular properties can be used to study different features of the processes involved in the transport of CRs. Other examples include<sup>21</sup>:

- Radioactive clocks: Some radioactive CR isotopes can be used as cosmic clocks, as their abundances relative to those of stable elements undergoing the same processes can reveal the timescale of the different phases in the CR life. Examples of this type of CRs are  $^{14}\text{C}$ ,  $^{10}\text{Be}$ , and  $^{54}\text{Mn}$ .
- Acceleration delay clocks: Some unstable primary isotopes decay only before their acceleration, so their abundance can be used to estimate the delay timescale between production and acceleration. Long delays would favor models where the cosmic-ray source is further away from acceleration sites. Examples of this type of CRs are  $^{59}\text{Ni}$ ,  $^{57}\text{Co}$  and  $^{56}\text{Ni}$ .
- Some unstable secondary isotopes also decay only while not accelerated. Since they are produced only after the acceleration and propagation of their primary CR sources, their presence can be used to determine if there were deceleration and subsequent re-acceleration phases during the CR propagation. Examples of this type of CRs are  $^{51}\text{Cr}$ ,  $^{52}\text{Cr}$ , and  $^{49}\text{Ti}$ .

### 1.4.3 Cosmic Rays in the Heliosphere

At the final stages of their travel toward the Earth, CRs are influenced by the solar wind.<sup>1</sup> The energy spectrum of CRs in the solar system is modulated for energies up to several  $GeV/n$ . This is due to a magnetized plasma in hydrodynamic expansion: the solar wind, a fully ionized gas, basically constituted of low energy electrons and protons ( $E \sim 0.5 MeV$ ), is pushed radially out of the Sun's corona, establishing a region of space in which the solar wind is dominant called heliosphere. Once the plasma has left the corona,

the dynamic pressure of this wind dominates over the magnetic pressure through most of the solar system, so that magnetic field lines are driven out by the plasma. The charged particles that penetrate the heliosphere are diffused and energetically influenced by the expanding solar wind: a schematic description of this phenomena is given in figure 5. The effect is that the least energetic CRs are shielded from the heliosphere, decreasing the flux below a few  $GeV/n$ . Furthermore, the intensity of solar activity and the solar winds have a time dependence and display an eleven-years cycle, so that the flux of low energies CRs is time-dependent.

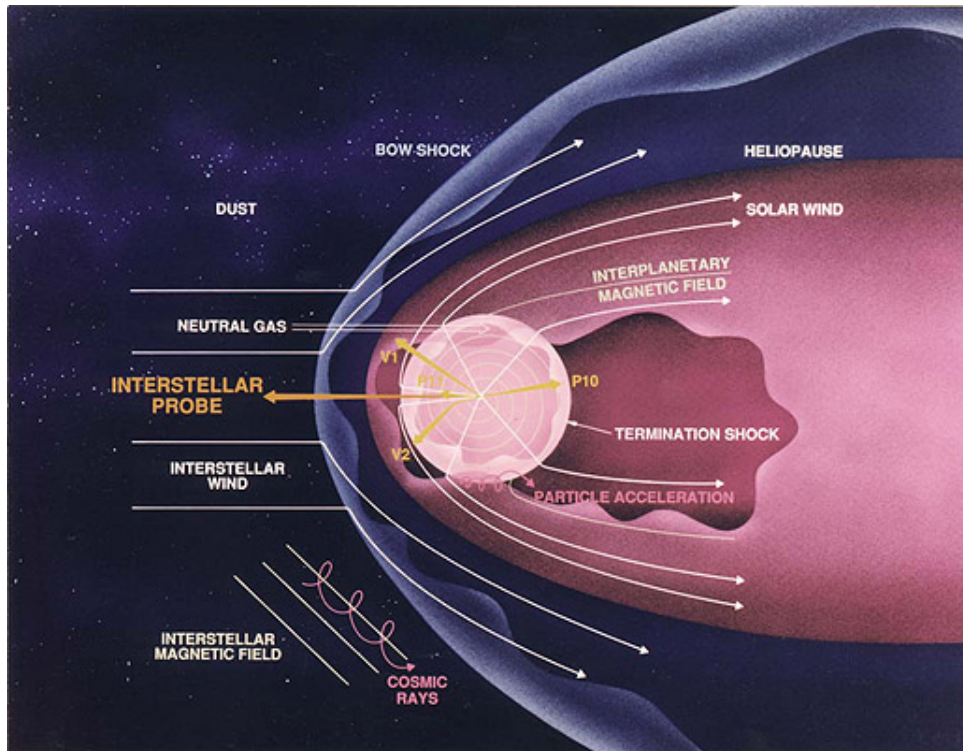


Figure 5 – Effect of Solar winds in the CRs.

Source: [VUKCEVIC<sup>24</sup>](#)

#### 1.4.4 Cosmic Rays in the Magnetosphere

The last obstacle that CRs have to overcome before reaching the Earth is the magnetosphere, i.e., the region of space surrounding the Earth in which charged-particles motion is affected by the Earth's magnetic field. The magnetosphere, together with the atmosphere, plays an important role in the development of life on Earth, as it mitigates the flux of CRs reaching Earth's surface.

To first approximation, the geomagnetic field can be represented as an offset and tilted dipole field with moment  $M = 8.1 \cdot 10^{25} \text{ Gcm}^3$ , an inclination of  $11^\circ$  relative to the axis of Earth rotation and a displacement of about  $400\text{km}$  from the Earth's center.<sup>5</sup>

Charged particles traversing the magnetic field experience the Lorentz force that produces a curved path. Thus CRs can be prevented from reaching an Earth-based detector, depending on their rigidity and incoming direction. The rigidity  $R$  of a charged particle is given by:  $R = pc/Ze$ , where  $p$  is the momentum of the particle,  $Ze$  its charge and  $c$  is the speed of light in vacuum. As a particle travels towards the Earth, its magnetic field will deflect the low rigidity particles, possibly preventing it from arriving altogether. For a given arrival direction and location there will exist a minimum value to the rigidity of a particle for which it will be allowed to penetrate the magnetosphere and be detected from Earth. This minimum rigidity value is called cut-off rigidity,  $R_C$ , and in the dipole approximation is given by:

$$R_C = \frac{M \cos^4 \lambda}{R_e^2 \left[ 1 + (1 \pm \cos^3 \lambda \cos \phi \sin \xi)^{\frac{1}{2}} \right]^2} \quad (1.2)$$

Where:

- $\lambda$  is the latitude from the magnetic equator;
- $M$  is the dipole moment;
- $\xi$  and  $\phi$  are, respectively, the polar angle from local zenith and the azimuthal angle counted clock-wise from local magnetic East;
- The  $\pm$  sign applies to negatively/positively charged particles;
- $R_e$  is the distance from the dipole center expressed in Earth radii units;

Particles detected with rigidity lower than the cut-off rigidity can be originated in the atmosphere of the Earth and be trapped in its magnetic field.

## 1.5 Deuterium Phenomenogy

Deuterium nuclei are rare in galactic CRs. No significant amount is expected to be released from galactic CRs sources since they are destroyed rather than formed in thermonuclear reactions inside stars. As a consequence of their production history, they are part of a class of secondary stable nuclei that provide information on the mean amount of matter traversed by CRs before escaping the galaxy. An important process by which they can be created in the Galaxy is nuclear fragmentation of CR nuclei with the gas of the ISM. The main production channel is from the spallation of  $^4\text{He}$  and with the resonant production  $p + p \rightarrow D + \pi$ . The deuterium production cross section for these reactions is known and shown in figure 6.

A compilation of the deuterium to hydrogen flux ratio measurements up to few GeV/nucleon is shown in figure 7. The first measurements of hydrogen and helium isotopes became available in the seventies, with energies up to 100 MeV/n. The identification,

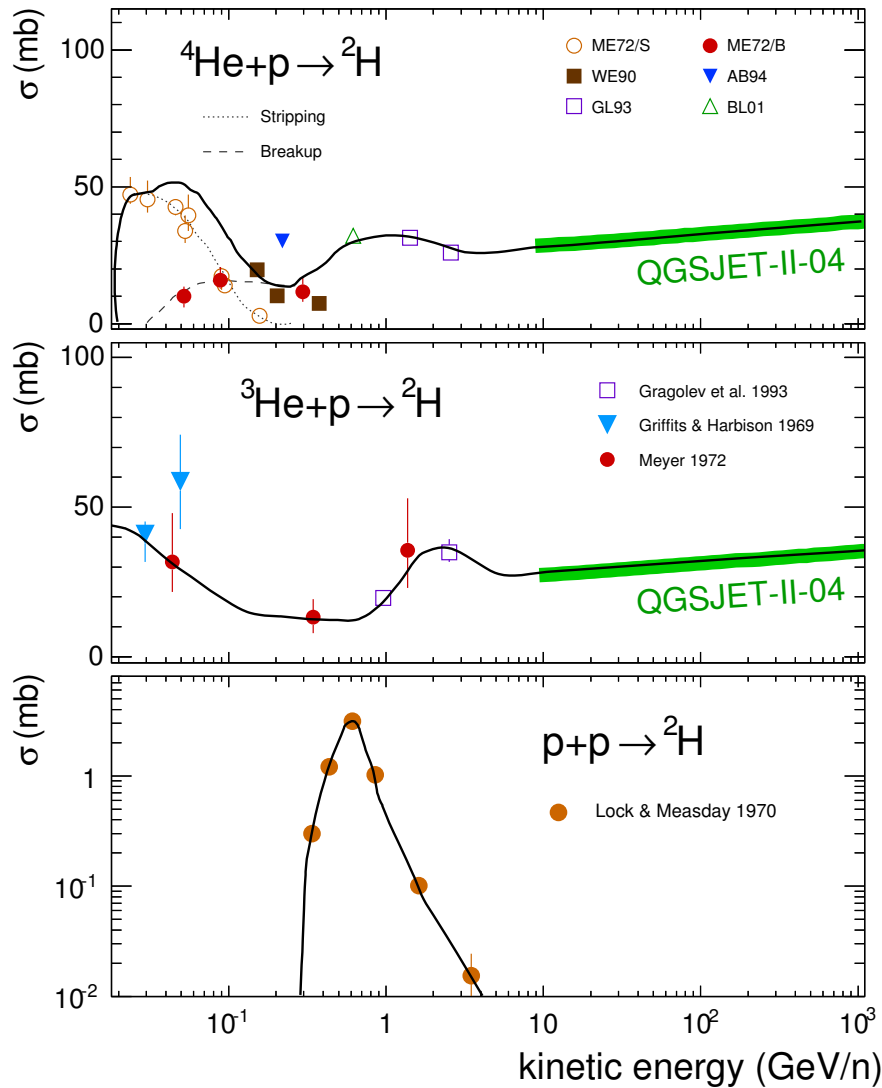


Figure 6 — Cross-section data for deuteron production from  ${}^4\text{He}-p$ ,  ${}^3\text{He}-p$ , and the resonant production.

Source: [TOMASSETTI et al.](#)<sup>25</sup>

especially at energies higher than 100 MeV/n, is quite difficult due to the high experimental mass resolution required to distinguish the secondary nuclei from the abundant background of primary hydrogen nuclei. In the eighties and nineties there have been several measurements of stratospheric balloon experiments using superconducting magnetic spectrometers<sup>27</sup> and also a measurement from AMS-01<sup>28</sup> in space. While the mass resolution of the balloon experiments was usually quite good, the residual atmosphere above the instruments caused a non-negligible background of secondary particles.

In the GeV-TeV energy region measurements of CR deuterium in these energies are very rare. Recently, an analysis of the SOKOL satellite<sup>29</sup> data provided the first measurements above 100 GeV/nucleon. The deuterium to proton ratio was evaluated as  $0.114 \pm 0.023$  for energies between 500 and 2000 GeV/n. The result from the SOKOL satellite cannot be

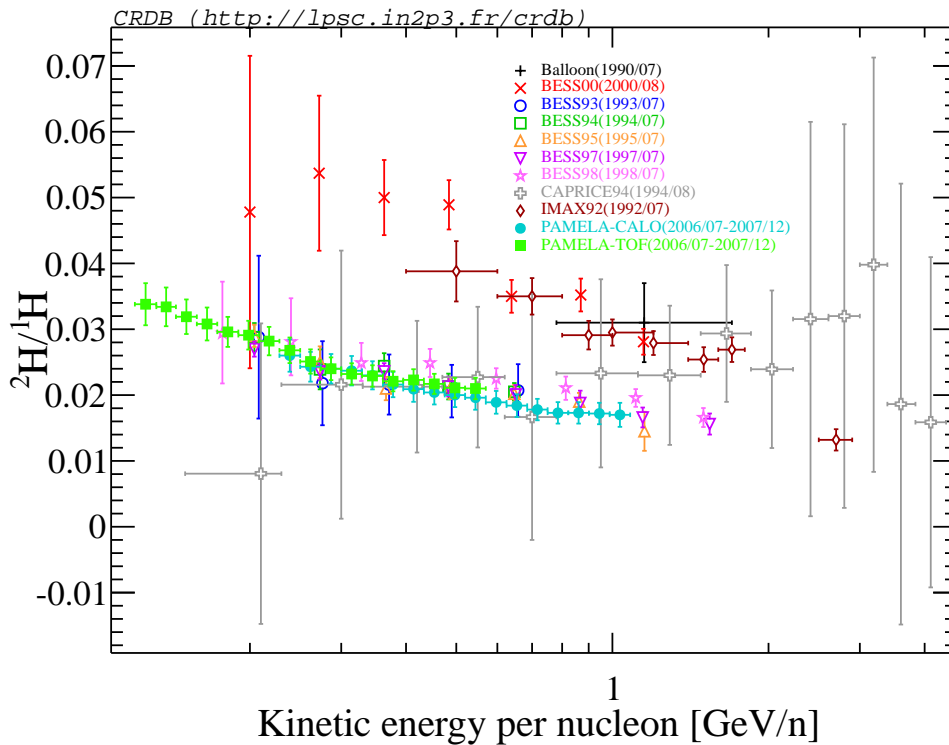


Figure 7 – Deuterium/proton ratio results for different experiments.

Source: MAURIN et al.<sup>26</sup>

explained by standard models of secondary CR production in the interstellar medium<sup>25</sup> and points to the existence of a high-energy source of CR deuterons, as can be seen in figure 8, showing the Boron-to-Carbon flux ratio and  ${}^2\text{H}/\text{He}$  ratio in view of two different CR scenarios. While B/C data are in good agreement with conventional propagation scenarios, the SOKOL measurement clearly disfavors these scenarios as the explanation for the  ${}^2\text{H}$  production, leaving doubts as to whether these secondaries nuclei have the same history.

In view of the implications of these recent results on the phenomenology of CR propagation, deuterium measurements performed with the AMS-02 detector become urgent. In this work we will present a measurement of the deuterium to hydrogen flux ratio between 0.7 to 7 GeV/n, obtained by analyzing the data collected by the AMS-02 experiment from May 2011 to May 2014.

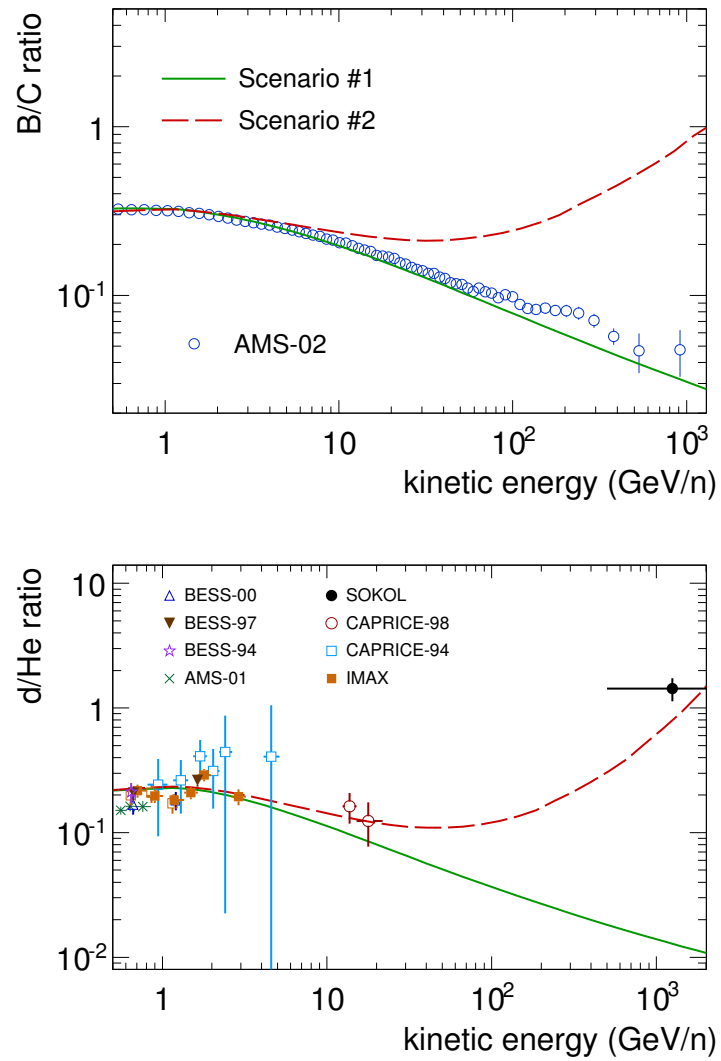


Figure 8 – Graphs comparing boron-to-carbon and deuteron-to-helium ratio measurements to the expected ratio according to different proposed CR scenarios.

Source: TOMASSETTI et al.<sup>25</sup>



## 2 THE ALPHA MAGNETIC SPECTROMETER

The Alpha Magnetic Spectrometer (AMS-02) is a large acceptance cosmic ray detector operating aboard the International Space Station (ISS) since 2011. The ISS follows a Low Earth Orbit at about 400 km altitude with respect to the Earth surface, well located to detect cosmic particles before they interact with the outer layers of the atmosphere. The data acquisition parameters of AMS-02 change as a function of the detector position with respect to Earth, as shown in figure 9. The average trigger rate is about 700 Hz, while the structures are due to the magnetic field of the Earth.

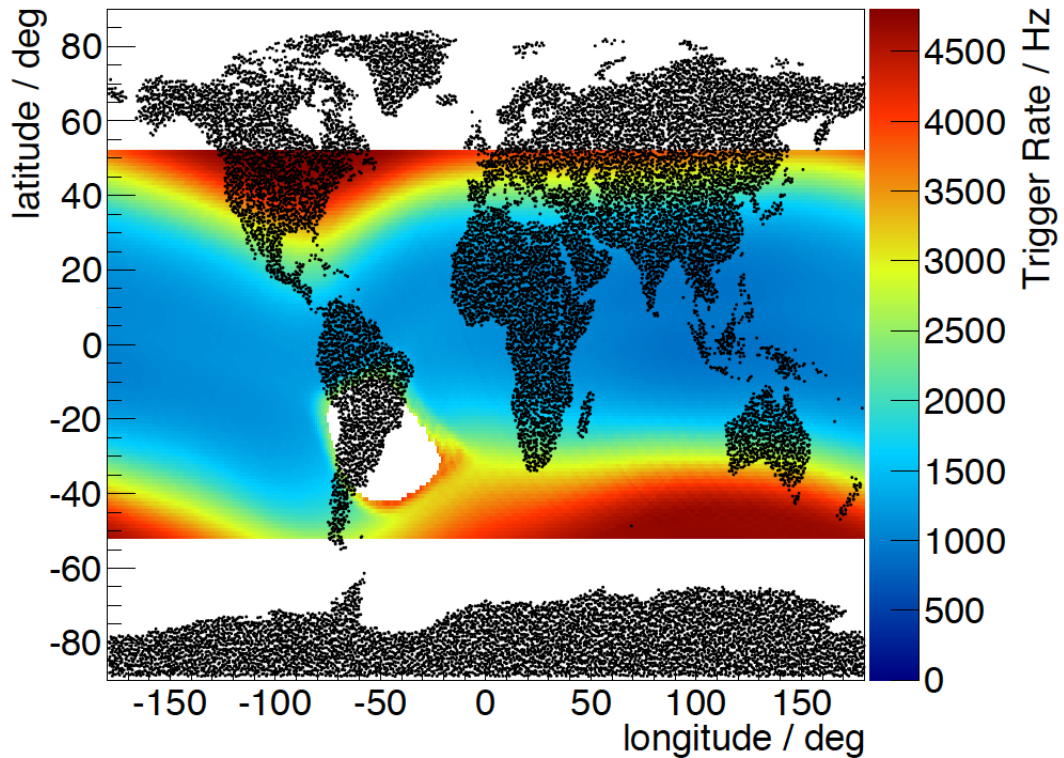


Figure 9 – Trigger rate of the AMS-02 experiment, as a function of the detector position with respect to the Earth.

Source: [TING<sup>30</sup>](#)

A schematic description of the detector is given in figure 10.<sup>31</sup> The silicon tracker measures the trajectory and absolute charge  $|Z|$  of cosmic rays by performing multiple measurements of the coordinates and energy loss. Together with the 0.14 T permanent magnet, the tracker measures the particle rigidity (momentum/charge). The Transition Radiation Detector (TRD) identifies the particle as an electron/positron. The four layers of the Time of Flight (TOF) measure the particles charge, velocity and ensure that the particle is downward-going. The high efficiency ( $\sim 99.999\%$ ) anti-coincidence counters

inside the magnet bore are used to reject particles outside of AMS's geometric acceptance. The Ring Imaging Cherenkov detector (RICH) measures the charge of the particle and its velocity. The imaging Electromagnetic Calorimeter (ECAL) identifies the particle as an electron/positron and measures its energy.

In the following a more detailed description of the sub-detectors that compose the AMS-02 experiment will be given.

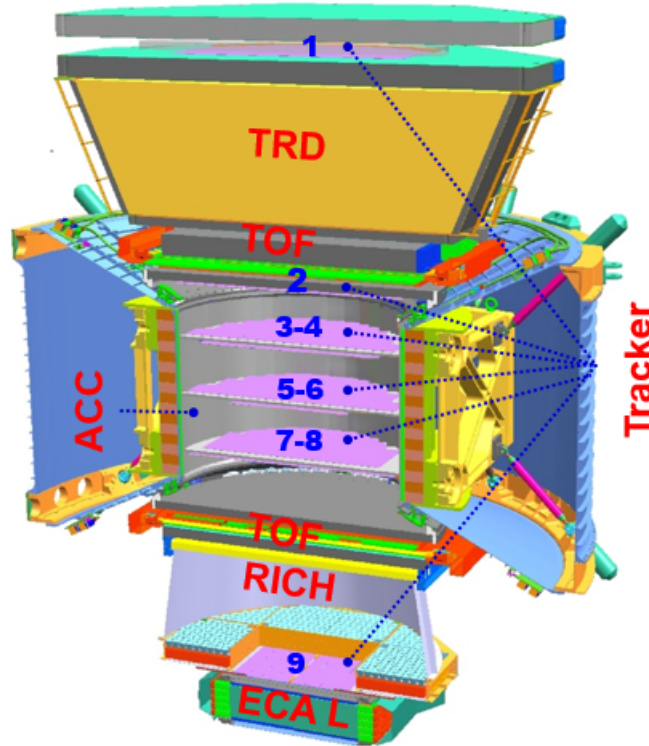


Figure 10 – Schematic view of AMS-02 sub-detectors.

Source: TING<sup>30</sup>

## 2.1 Transition Radiation Detector

The AMS-02 Transition Radiation Detector (TRD)<sup>32</sup> is used to perform lepton/hadron separation as well as to provide a redundant charge measurement. Transition Radiation (TR) X-rays are emitted by charged particles when crossing the boundary between two media with different dielectric constants, as shown in figure 11. The probability of photon emission is negligible for values of the Lorentz boost factor  $\gamma < 1000$ , while above this threshold, it is nearly independent of the velocity, but only on the particles absolute charge  $\sim 0.005 \cdot Z^2$ . The low production rate at the single boundary crossing is overcome by a stack of radiator foils, i.e., multiple vacuum-matter interfaces, interleaved with proportional tubes. Being sensitive to the  $\gamma$  of incident particles, TRD detectors are typically used to discriminate between relativistic electrons and protons up to several

hundred  $GeV$ , since electrons, compared to protons with the same energy, have a much higher Lorentz boost factor and therefore emit more TR. Also, while a similar Lorentz factor characterizes nuclei with the same kinetic energy per nucleon ( $\gamma - 1 = K/m$ ), the number of emitted photons varies significantly in different species, and the energy deposition due to minimum ionizing nuclei can also be used to infer the magnitude of their charge up to carbon. The TRD has also tracking capabilities with a resolution at the  $mm$  level.

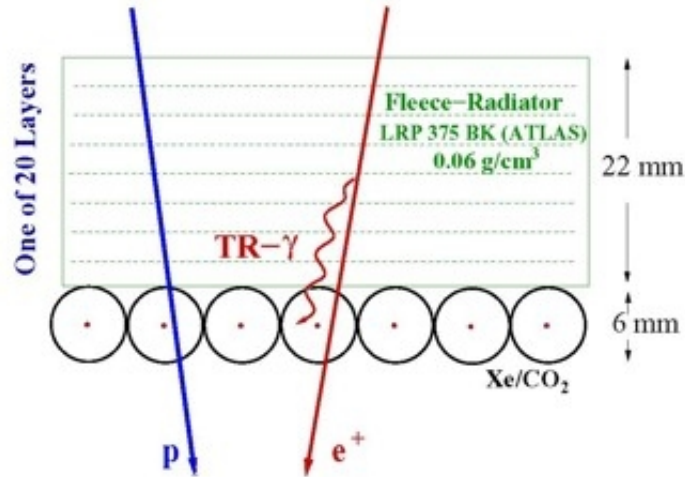


Figure 11 – AMS-02 TRD detection principle - charged particles with high  $\gamma$  passing through the radiator emit  $\gamma$  rays that are detected in the Xe/CO<sub>2</sub>.

Source: [DOETINCHEM et al.](#)<sup>33</sup>

The AMS-02 TRD, shown in figure 12, is made of 328 modules arranged in 20 layers along the vertical coordinate. Each module contains: 20 mm of radiator made of polypropylene/polyethylene fiber fleece corresponding to  $0.06 g/cm^3$ , 16 tube straws filled with a Xe:CO<sub>2</sub> (80%:20%) gas mixture. As the TR X-rays enter the tubes straws it ionizes the gas inside and starts an ionization avalanche in the proximity of a thin wire at high voltage, 1600 V, on full avalanche regime. This abrupt current change induces a fast electric signal that can be read out at the end of the wire. The X-ray ionization signal adds up to the normal ionization of charged particles traversing the gas. The large number of interfaces (hundreds) increases the probability of production of X-rays.



Figure 12 – AMS-02 TRD.

Source: [DOETINCHEM et al.](#)<sup>33</sup>

## 2.2 Time Of Flight

The AMS-02 Time Of Flight (TOF) system<sup>34</sup> is composed of four planes of scintillation counters, two above (Upper TOF) and two below (Lower TOF) the inner tracker. They measure the time of flight (i.e., the particle velocity), to provide a trigger for the whole experiment and to provide the measurement of the particle charge. The TOF upper and lower planes are shown in figure 13. Charged particle ionization in the scintillating medium causes molecular excitation and de-excitation with the fast emission ( $\tau \sim 10^{-8} s$ ) of fluorescence light. The photon collection provides a very precise hit time measurement and an estimation of the particle's energy deposit, which gives an evaluation of the particle charge exploiting the relation between the energy loss by ionization ( $\propto Z^2$ ) and the produced scintillation light for every single ToF counter.

The four planes contain, from top to bottom, eight, eight, ten and eight scintillator paddles. A single counter is shown in figure 14. Each counter is made of 1cm-thick polyvinyl-toluene scintillators. Each end is coupled by means of plexiglass guides to photomultiplier tubes (PMTs). The paddles are alternatively positioned along  $x$  and  $y$  to provide a bi-dimensional measurement with a granularity of  $12 \times 12 cm^2$ .

The timing resolution of the TOF is  $\approx 180 ps$  for  $Z=1$  particles and  $\approx 100 ps$  for  $Z \geq 2$ . The resulting resolution on velocity  $\beta$  is  $\sigma_\beta/\beta \approx 4\%$  (at  $\beta = 1$ ) for  $Z=1$  and  $\approx 1\%$  for other ions. This resolution gives a distinction power between upward-going and downward-going nuclei  $> 10^{10}$ .



Figure 13 – The Upper and Lower TOF in a assembly test before the integration in AMS.

Source: [VAGELLI<sup>35</sup>](#)

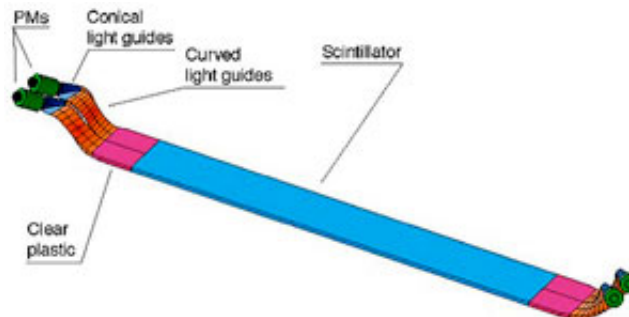


Figure 14 – Design of a TOF paddle.

Source: [VAGELLI<sup>35</sup>](#)

## 2.3 Tracker

The AMS-02 tracker<sup>36,37</sup> is composed of nine layers of double-sided silicon microstrip sensor arranged along the height of the AMS-02 detector. Layers 1 and 9 constitute the external tracker and are positioned at both ends of the AMS-02 detector, above the TRD and the ECAL respectively, to maximize the lever arm in the trajectory determination. Layers 2 to 8 constitute the inner tracker and are arranged in a permanent magnet structure that provides a  $0.14T$  magnetic field for bending charged-particle trajectories. While layer 2 sits right above the magnet, layers 3-8 are supported by three carbon fiber and aluminum

planes inside it and are placed in pairs (3-4, 5-6, 7-8), with a relative distance between layers belonging to the same plane of  $\approx 4\text{cm}$ . The most inner plane (layers 5-6) is placed at the center of the magnet and the two neighbors symmetrically disposed at  $z = \pm 27\text{ cm}$  from the central one. Each layer contains a variable number (around 20) of read-out units, called ladder, each ladder having a variable number (from 10 to 15) of silicon sensors. The total active area of  $6.4\text{m}^2$ , with a total number of 2284 Silicon sensors arranged in 192 ladders, makes the AMS-02 Silicon Tracker the largest tracker for a magnetic spectrometer ever built for space application. Figure 15 shows the trackers planes.

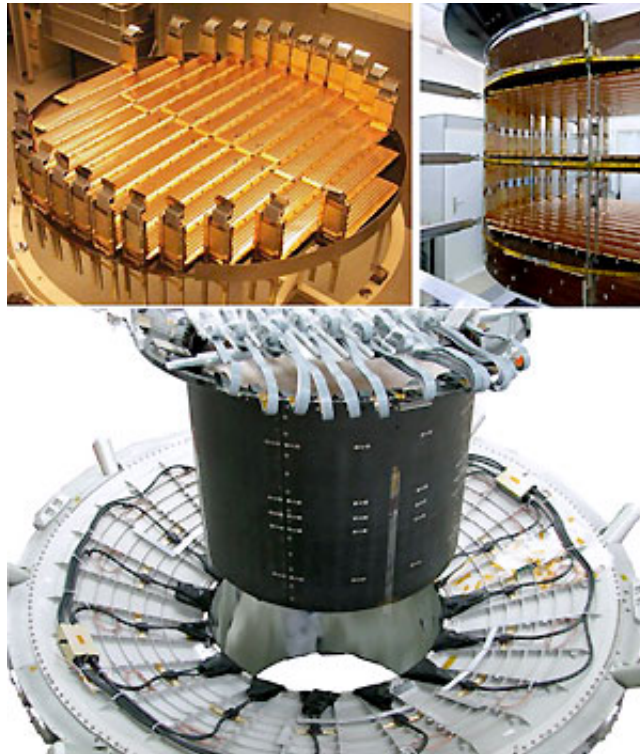


Figure 15 – An AMS Silicon Tracker picture gallery. Left, a single Tracker plane. Right, 5 planes mounted on the Tracker support. Bottom, the integration of the Tracker into the AMS-02 magnet at CERN.

Source: DURANTI<sup>38</sup>

When an ionizing particle crosses the silicon detector, electron/hole pairs ( $\sim 10^4$ ) are produced. Charges are rapidly drifted ( $\tau \sim 10\text{ns}$ ) by the sensor's electric field, generated by an inverse bias regime, toward the segmented electrode strips. The obtained signal is proportional to the energy deposit and identifies the coordinate of the traversing particle. From the hit coordinates, a track of the particle is reconstructed. The curvature of the track measures the particle's rigidity, while the energy deposited in each layer measures independently its charge magnitude. Each hit records bending( $Y$ ) and non-bending( $X$ ) coordinates, with a single point precision of  $10\ \mu\text{m}$ , as well as two measurements of the specific energy loss  $dE/dx$ . The measured spatial resolution of  $10.7\ (6.5)\ \mu\text{m}$  for protons (helium) for the bending coordinate gives a Maximum Detectable Rigidity (MDR), the

rigidity associated with a 100% measurement error, of few  $TV$  (2  $TV$  for protons and 3.2  $TV$  for helium).<sup>37</sup>

## 2.4 Ring Imaging Detector

The AMS-02 Ring Imaging Cherenkov detector<sup>39</sup> (RICH) is located between the Lower TOF and the ECAL and consists of a radiator plane, where Cherenkov light is emitted, a conical, high reflectivity conical mirror surrounding the expansion volume, and a detection plane made of a matrix of photomultiplier tubes and light guides.

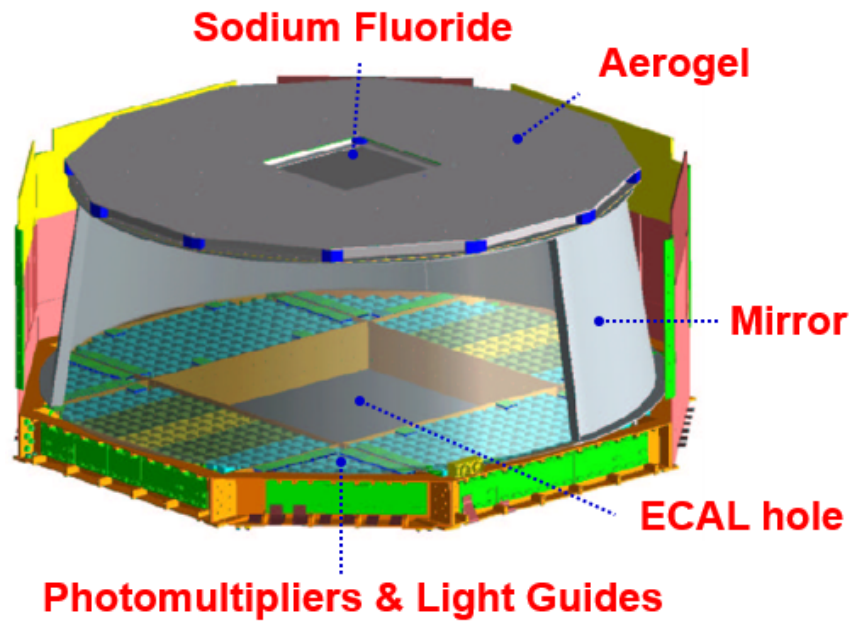


Figure 16 – AMS-02 RICH sub-detector

Source: GILLARD<sup>39</sup>

The detection plane has a hole at the center to minimize the amount of material in front of the ECAL. The detector layout is shown in Figure 16, while Figure 17 shows the detection principle.

Cherenkov radiation is emitted by a charged particle while traversing a transparent medium with superluminal velocity. Coherent radiation is emitted along the surface of a cone, whose properties depend on the velocity of the particle as well as on the refractive index  $n$  of the traversed medium. The minimum velocity of the particle for the emission of the radiation,  $\beta_{thr}$ , is given by  $\beta_{thr} = 1/n$  and the aperture angle of the cone is known as the Cherenkov angle,  $\theta_C$ , and relates to  $n$  and  $\beta$  by  $\beta = \frac{1}{n \cos(\theta_C)}$ .

The radiator plane includes two different radiators: 16 squared tiles of Sodium Fluoride, NaF, ( $n = 1.334$ ) with dimensions  $8.5 \times 8.5 \times 0.5 \text{ cm}^3$  in the center covering  $\sim 10\%$  of the RICH acceptance, and 92 silica aerogel ( $n = 1.05$ ) tiles with dimensions  $11.5 \times 11.5 \times 2.5 \text{ cm}^3$

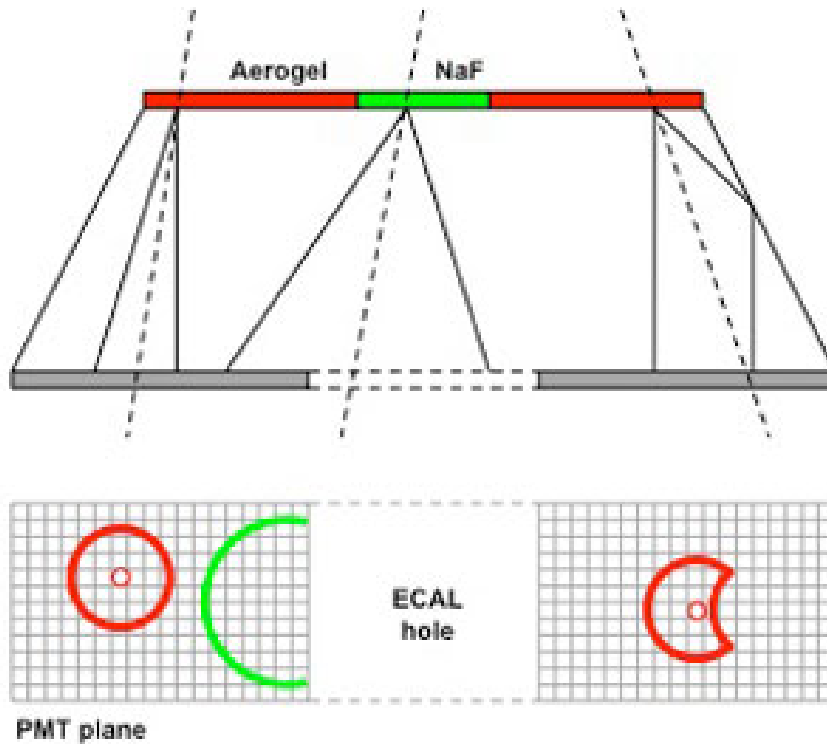


Figure 17 – AMS-02 RICH detection scheme

Source: [AMS-02](#)<sup>40</sup>

surrounding the NaF radiator. The Cherenkov threshold for aerogel is  $\beta = 0.95$ , while for NaF, it is  $\beta = 0.75$ . The purpose of the NaF radiator is that, since particles passing through it will generate Cherenkov radiation with a larger Cherenkov angle, it projects the cone of light out of the way of the hole in the detection plane on top of the ECAL, increasing the acceptance of the detectors for particle trajectories pointing towards the ECAL.

The measurement of the opening angle of the Cherenkov cone is done by the detection of a Cherenkov ring in the imaging detector. The velocity of the particle can then be measured and the estimation of the number of detected photons provide an independent measurement of the charge of the incoming particle. A measurement of the velocity at the per mille level is mandatory to remove the low-energy background pions generated in the interactions with the detector material and to measure the composition of light isotopes. RICH provides measurement of  $\beta$  with a resolution  $\sigma_\beta/\beta \sim 0.1\%$ , for single-charged particles, and  $\sigma_\beta/\beta \sim 0.01\%$  for other ions. It also provides a measurement of the charge of the particle with a charge confusion of the order of 10%.

## 2.5 Anti-Coincidence Counter

The Anti-Coincidence scintillator Counter (ACC) system<sup>41</sup> surrounds the tracker planes installed within the magnet volume: it provides the veto signal to the trigger in order to reject multi-particle events generated by the interaction of cosmic rays entering the detector through the sides.

The ACC is composed of 16 paddles, the light coming from both ends of each scintillator is collected by wavelength shifter fibers of 1 mm diameter, embedded in grooves milled into the scintillation panels. The fibers are arranged in bunches of 37 fibers and brought outside the magnet bore where are read by 16 PMTs (eight in the upper part of the magnet and eight in the lower, to provide redundancy), similar to the ones used for TOF. The system is designed to have a very low inefficiency (below 1/300000), and the high degree of homogeneity of the scintillating fibers ensures a reliable and fast signal for the high inclination particles with also some impact point determination capabilities.

## 2.6 The Electromagnetic Calorimeter

When a high-energy  $e^+$ ,  $e^-$  or  $\gamma$  passes through a material with a high  $Z$  -as Lead- many other  $e^+$ ,  $e^-$  and  $\gamma$  of lower energy are produced. This particle production is called electromagnetic shower and is caused by the interplay of two phenomena: the bremsstrahlung, the electromagnetic radiation produced by the deceleration of a charged particle when deflected by another charged particle, and pair production, the creation of an elementary particle and its antiparticle from a photon. The shower ends either when secondary particles are absorbed in material or when they can escape from the material. An incident proton interacts in a very different way, as we can see in figure 18.

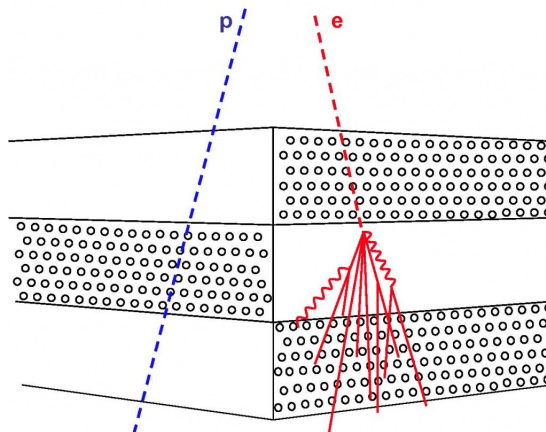


Figure 18 – Schematic description of the passage of a proton and an electron through the ECAL.

Source: VAGELLI<sup>35</sup>

The ECAL<sup>42</sup> is located at the bottom of the AMS-02 detector. It is a fine grained

sampling calorimeter, made of lead and scintillating fibers, that provides a tridimensional imaging of the longitudinal and lateral shower development. The 3D shower profile is reconstructed using the information of 18 longitudinal and 72 lateral measurements. The accurate description of this longitudinal and transverse shower shape allows lepton/hadron separation. It has an angular resolution of  $\sim 1^\circ$  and provides a stand-alone photon trigger capability to AMS.

The mechanical structure of the calorimeter, shown in Figure 19, is a square parallelepiped divided into nine super-layers (see Figure 20). Each super-layer, 18.5mm thick, consists of 11 grooved lead foils, 1mm thick, interleaved with layers of 1mm diameter scintillating fibers. In each super-layer fibers run along the same direction: the 3-D imaging capability is obtained by stacking super-layers with fibers alternatively parallel to Y-axis (4 layers, X-view) and X-axis (5 layers, Y view). The resulting composite structure has an average density of  $6.8\text{g/cm}^3$ , and the total calorimeter thickness corresponds to almost 18 radiation lengths. The high granularity permits a high rejection power between electrons and hadrons: each square element (9mm side) corresponds to half Molière radius in transverse dimensions and one radiation length in depth.



Figure 19 – The Electromagnetic Calorimeter brick before the final integration. PMTs are lodged on the square holes.

Source: [VAGELLI](#)<sup>35</sup>

A proton rejection of the order of  $\sim 10^6$  is achieved by combining the TRD and the tracker the ECAL.<sup>35</sup>



Figure 20 – ECAL active volume (pancake). Nine superlayers are piled-up for a total of 50,000 1 mm scintillating fibers running in opposite directions. The total  $68.5 \times 68.5 \times 16.7 \text{ cm}^3$  pancake volume consists of a lead-fiber-glue volume ratio of 1:0.57:0.15, for an average density of  $\sim 6.8 \text{ g/cm}^3$ .

Source: [VAGELLI<sup>35</sup>](#)



### 3 MEASUREMENT OF COSMIC RAY PROPERTIES WITH AMS-02

The AMS-02 experiment has been designed to allow the precise measurement of CR particles in the GeV to TeV energy range, by using several detection techniques widely used in particle physics experiments.<sup>43</sup> In this chapter, we will describe how some of the CR properties, namely the particle charge, momentum and mass can be measured by means of the signals collected in the sub-detectors that compose AMS-02.

#### 3.1 Charge Measurement

Among charged CR species, AMS-02 can measure relative abundances and absolute fluxes of CR nuclei from hydrogen up to at least iron, in a kinetic energy range from hundreds of *MeV* to *TeV* per nucleon. The measurement of the chemical composition of CRs with high statistics in this extended energy range will reveal new insights about the CR life in the galaxy, from their origin to the propagation in the interstellar medium, giving new constraints to astrophysical models of GCRs.

The absolute charge  $Z$  of a nucleus is measured several times along the trajectory of the particle inside AMS-02 using different detection techniques<sup>44</sup>: in the nine planes of the silicon tracker, in the four layers of scintillator counters of the TOF, in the RICH, in the 20 layers of the TRD, and in the upper layers of the ECAL. Figure 21 shows the charge response of single sub-detector units to light CR elements, from hydrogen to oxygen.

In the following, we will outline the principles of the charge measurements for the tracker and the time of flight, that are used to identify the charge magnitude of the deuterium and hydrogen events.

##### 3.1.1 Tracker

The silicon tracker of the AMS-02 detector is used for the measurement of cosmic ray momentum and charge, together with the sign of the charge, identified using the permanent magnet. The charge magnitude is estimated through the energy-loss measurement while crossing the silicon. The tracker response to nuclei from helium up to the iron group has been studied by exposing the detector to ion beams at CERN and GSI.<sup>45</sup> The energy loss while crossing the material is given by the Bethe-Block formula<sup>43</sup>:

$$-\frac{dE}{dx} = K z^2 \frac{Z}{A} \frac{1}{\beta^2} \left[ \frac{1}{2} \ln \frac{2m_e c^2 \beta^2 \gamma^2 T_{max}}{I^2} - \beta^2 - \frac{\delta(\beta\gamma)}{2} \right], \quad (3.1)$$

where:

- $x$  is the amount of traversed material in  $g/cm^2$ ;

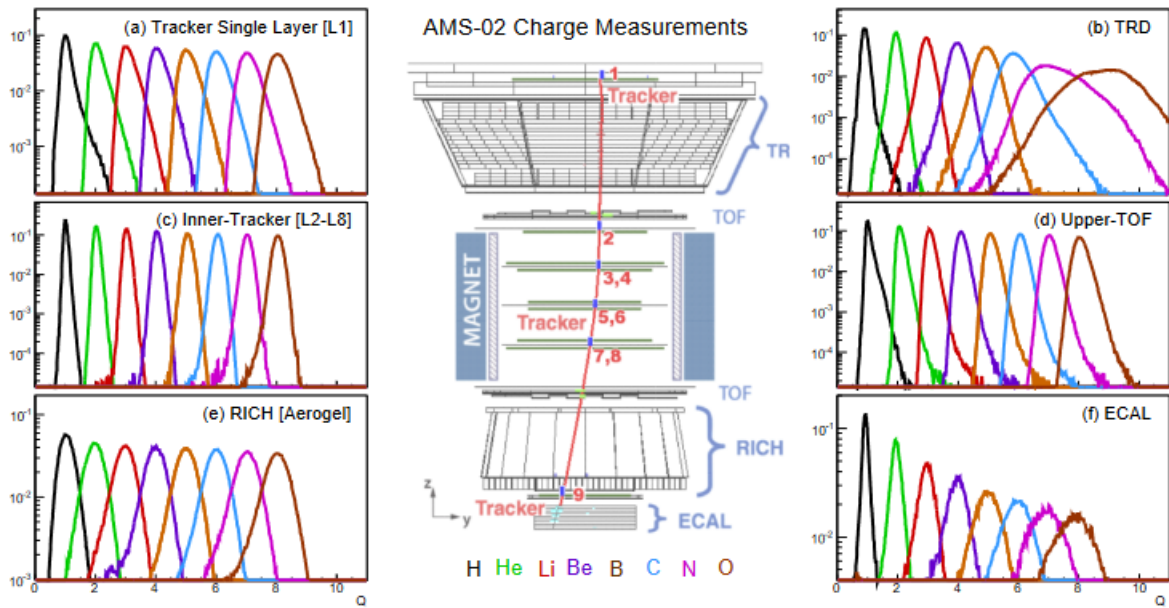


Figure 21 – Schematic Y-Z view of the AMS-02 detector, illustrating the path of a typical CR event. The panels show the charge response of single sub-detector units to light CR elements ( $Z = 1$  to  $Z = 8$ ): (a,c) Tracker, (b) TRD, (d) TOF, (e) RICH, and (f) ECAL.

Source: TOMASSETTI et al.<sup>44</sup>

- $K \simeq 0.307 \text{ MeVg}^{-1}\text{cm}^2$ ;
- $Z$ ,  $A$  and  $I$  are characteristics of the traversed material and correspond to the atomic number, the mass number and the mean excitation energy;
- $z$ ,  $\beta$  and  $T_{max}$  are the charge of the incoming particle, speed and maximum energy transferable in a collision with an electron;
- $\delta(\beta\gamma)/2$ , is a density-effect correction.

Indicating with  $H$  the energy loss for a Minimum Ionizing Particle (MIP) and applying the usual approximations of the Bethe-Block formula results:

$$-\frac{dE}{dx} \approx Hz^2. \quad (3.2)$$

Considering a  $300\mu\text{m}$  silicon sensor the average MIP energy loss in the AMS-02 silicon tracker results  $H_{300\mu\text{m},\text{Si}} \simeq 80\text{keV}$ .

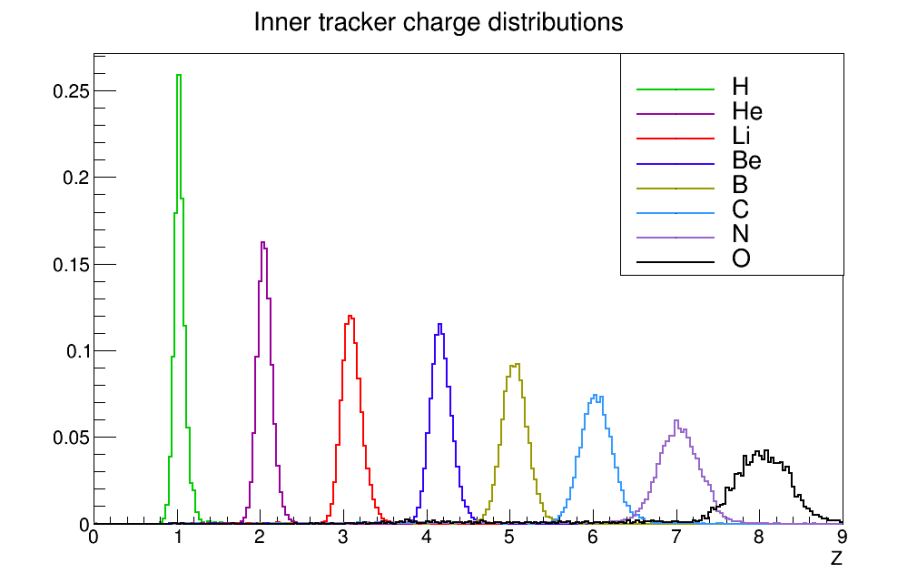


Figure 22 – Charge distribution for simulated events detected by the inner tracker.

Source: By the author

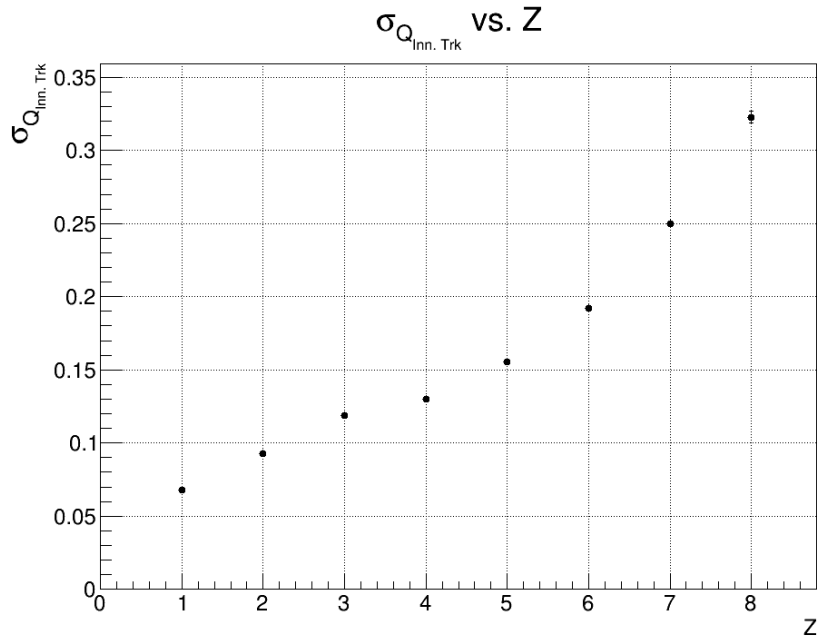


Figure 23 – Charge resolution for simulated events detected by the inner tracker: each point corresponds to the gaussian width of the distributions in Figure 22.

Source: By the author

### 3.1.2 Time of flight

The scintillation light produced by particles traversing a plastic scintillator is related to the energy deposited by ionization, as described above, and is given by the

empirical formula<sup>34</sup>:

$$L = \frac{AdE/dx}{1 + BdE/dx + C(dE/dx)^2} \quad (3.3)$$

where  $A$ ,  $B$  and  $C$  are constants determined experimentally. Typical values for AMS scintillators are  $A \approx 10 \text{ MeV}^{-1}\text{cm}$ ,  $B \approx 10^{-2} \text{ MeV}^{-1}\text{cm}$  and  $C \approx 10^{-5} \text{ MeV}^{-2}\text{cm}^2$ . The specific energy loss,  $dE/dx$ , for different types of particle can be calculated using the Bethe-Block formula discussed above and is proportional to the square of the charge. Given the small values of  $B$  and  $C$ , the scintillation light is roughly proportional to  $Z^2$ , and an efficient charge separation can also be done with TOF. However, saturation effects and the details of the light transportation in the scintillator introduce a degradation of the charge separation power for  $Z \geq 10$ .

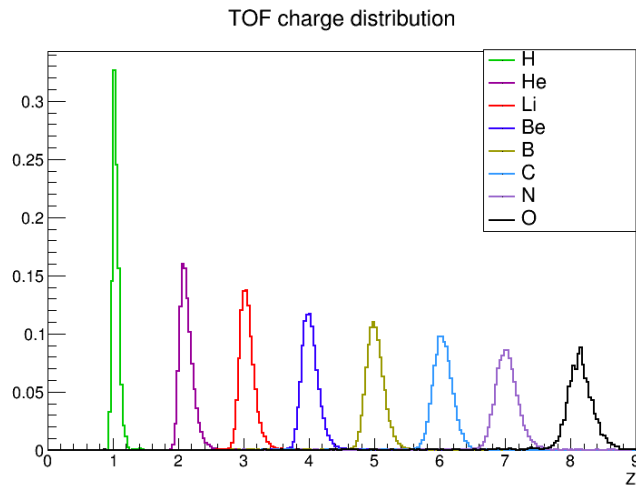


Figure 24 – Charge distribution for simulated events detected by the TOF.

Source: By the author

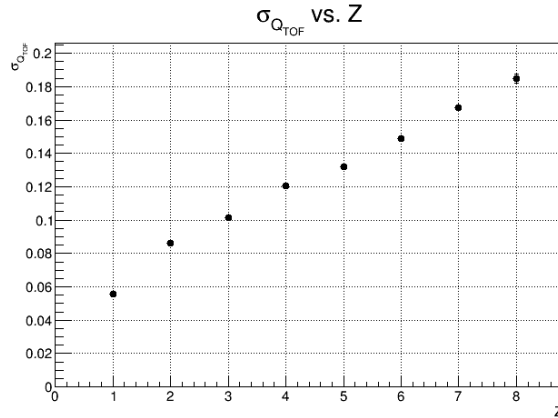


Figure 25 – Charge resolution for simulated events detected by the TOF: each point corresponds to the gaussian width of the distributions in Figure 24.

Source: By the author

### 3.2 Momentum Measurement

The silicon tracker, together with the magnet, measures the momentum and the sign of the charge of cosmic rays, providing accurate measurements in the range from 0.5 GV to several TV. The AMS-02 tracker measures the magnetic rigidity  $R$  of each event, given by:

$$R = \frac{pc}{Ze} = \frac{\gamma m \beta c^2}{Ze}, \quad (3.4)$$

where  $p$  is the particle momentum,  $Z$  is its atomic number,  $c$  is the speed of light in the vacuum,  $e$  is the elementary charge,  $m$  is the particle's mass,  $\beta$  its velocity and  $\gamma$  the Lorentz boost factor. The rigidity measurement relies on the reconstruction of the particle track as it passes through the layers of the tracker. After the track is reconstructed, its curvature can be used to determine the rigidity. The curvature is related to the magnetic field and the momentum by equating the Lorentz force of the charged particle with the centripetal force of a circular motion:

$$\frac{qpB}{m} = \frac{p^2}{mr} \rightarrow Br = p/q = R/c. \quad (3.5)$$

In natural units we get:

$$R = Br. \quad (3.6)$$

A schematic description of the particle traversing the silicon tracker is given in Figure 26, where  $r$  is the curvature of the trajectory,  $S$  is the sagitta,  $L$  is the distance between the external planes,  $\theta$  is the angle of the circular sector, in the approximation of small angles. Following conventions presented in Figure 26, we have:

$$L = 2r \sin \frac{\theta}{2} \approx r\theta \quad (3.7)$$

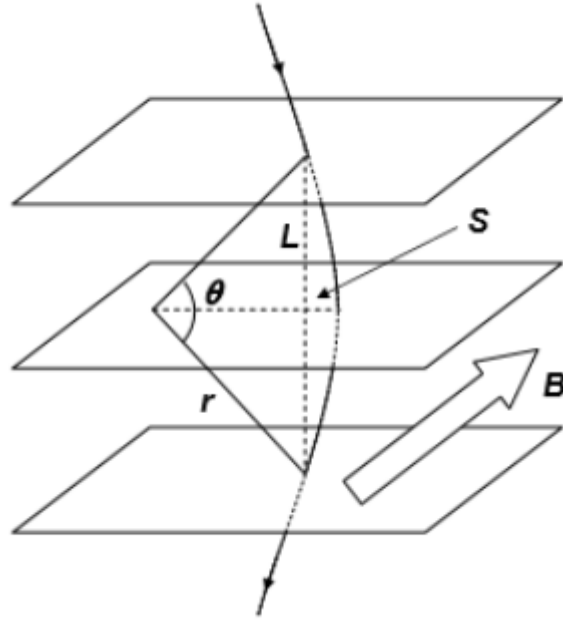


Figure 26 – A schematic description of the particle traversing the silicon tracker:  $r$  is the curvature of the trajectory,  $S$  is the sagitta,  $L$  is the distance between the external planes,  $B$  is the magnetic field and  $\theta$  is the angle of the circular sector, in the approximation of small angles.

Source: LEO<sup>43</sup>

and

$$S = r \left( 1 - \cos \frac{\theta}{2} \right) \approx r \frac{\theta^2}{8} \quad (3.8)$$

Using 3.6 and 3.7 in 3.8 we obtain:

$$S = \frac{BL^2}{8R} \quad (3.9)$$

The sagitta  $S$  is the quantity directly measured by the tracker by which we can calculate the rigidity. Considering a minimum of three points  $x_1$ ,  $x_2$  and  $x_3$  for the determination of the sagitta,

$$S = x_2 - \frac{x_1 + x_3}{2} \quad (3.10)$$

and:

$$\sigma_S = \sqrt{\frac{3}{2}} \sigma_x. \quad (3.11)$$

From the relation  $S = BL^2/8R$ , sagitta and rigidity have the same relative error, resulting:

$$\frac{\sigma_R}{R} = \frac{\sigma_S}{S} = \sqrt{\frac{3}{2}} \frac{8R}{BL^2} \sigma_x \quad (3.12)$$

The information on the magnetic field strength allows the reconstruction of the charged particle track and consequently the measurement of the CR rigidity.

The AMS-02 analysis software allows for multiple rigidity measurements, that can be

obtained by taking into account the hits detected in several tracker layers.<sup>37</sup> Combining the multiple hits in the nine layers of the silicon tracker we can obtain multiple combinations of layers to measure the rigidity. A “span” is the configuration used to perform the track fit. The more detailed rigidity measurement is obtained by requiring that all the tracker layers have detected hits. This configuration is called “full tracker span” rigidity: hits in the nine layers are used to fit a track. This configuration has the advantage of having better accuracy on the rigidity measurement, but the disadvantage that fewer events passing through AMS will hit all layers, so the corresponding fraction of events that can be reconstructed is lower than others. The “inner tracker” span only uses the layers 2 to 8, to make this measurement, so its acceptance is increases. This configuration shows good performance below 80 GV, however it cannot be used above this threshold due to the limited detector size. A "maximum tracker span" corresponds to the track fit with all the available information, so it constitutes an intermediate solution regarding available statistics and rigidity measurement accuracy.

Simulated events can be used to evaluate the rigidity resolution, by studying the quantity  $(1/R_{rec} - 1/R_{gen})/(1/R_{gen})$  as a function of the generated rigidity  $R_{gen}$ . For each individual rigidity bin, the resolution distribution is fitted to a combination of three gaussian functions.<sup>38</sup> In the absence of experimental biases the three gaussian functions should be centered at zero. For each rigidity bin, the resolution is given by the weighted mean of the gaussian mean values, the weights being the areas of the gaussian distributions. Figure 27 shows an example obtained by analyzing simulated helium events for a given rigidity bin. The tracker rigidity resolution for simulated helium events has been estimated for both the "inner tracker span" and the "full tracker span," and the corresponding results are shown in Figure 28. As expected, the rigidity resolution is around 10% below 10 GV, because of the multiple scattering. We can see that the two configurations provide compatible results below 80 GV. Above this region, the inner tracker is no longer much useful for the rigidity measurement as its resolution increases, due to its limited lever arm. After reaching a minimum around 10 GV the resolution increases up to the Maximum Detectable Rigidity (MDR), corresponding to 100% uncertainty on the resolution measurement. Considering a spatial resolution of  $\sim 10.7$  (6.5)  $\mu m$  for protons (helium) in the bending direction and a bending power  $BL^2 = 0.87 Tm^2$ , a MDR of 2.2 (3.7) TV and a rigidity resolution of  $\sim 10\%$  up to GV rigidities are obtained. Our result is compatible with the official AMS-02 result.<sup>46</sup>

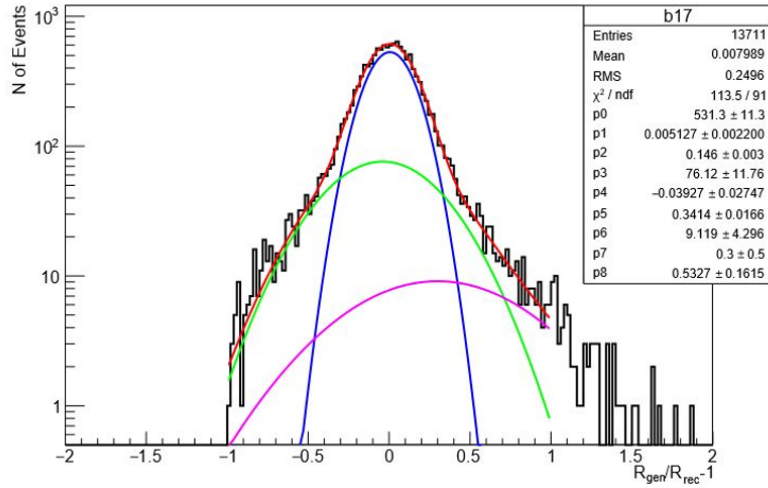


Figure 27 – Rigidity resolution for simulated helium events for a given rigidity interval, namely  $95.5 \text{ GV} < R < 123 \text{ GV}$ . The distribution is fitted by the sum of three gaussian functions.

Source: By the author

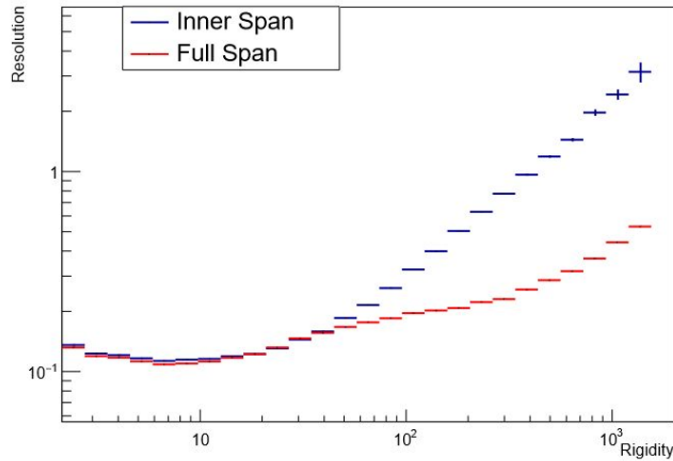


Figure 28 – Rigidity resolution for the "full tracker" span and "inner tracker" span.

Source: By the author

### 3.3 Mass measurement

The mass and the isotopic composition of cosmic-ray nuclei can be performed by the AMS-02 experiment using the measurements of the momentum and velocity of the particles. Over the sample of well-reconstructed events, we can perform mass separation at a given rigidity, since the mass of the particles is given by:

$$m = \frac{RZe}{\gamma\beta c} \quad (3.13)$$

where  $R$  is the CR rigidity measured by the silicon tracker,  $Ze$  is the particle charge,  $\gamma$  is the Lorentz factor and  $\beta$  is particle velocity measured by the TOF or the RICH. The quantity  $1/m$  is measured instead of the actual mass because the silicon tracker measures the inverse of rigidity with the sagitta method, as discussed in previous sections. Figures 29 and 30 show some examples of the  $1/m$  distribution for well-reconstructed single-charged events detected by the AMS-02 detector, for two kinetic energy bins for events whose velocity is measured by the RICH-NaF radiator as well as by the RICH-aerogel radiator.

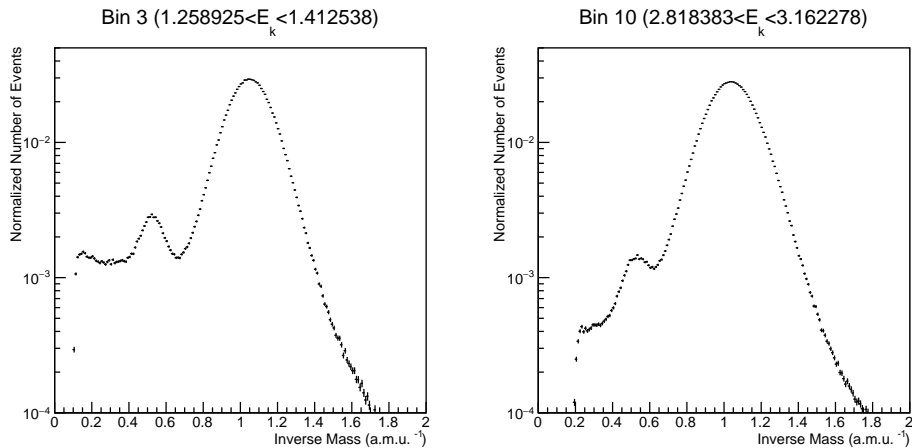


Figure 29 – The  $1/m$  distribution for two kinetic energy, measured in GeV/n, bins, for events whose velocity is measured by the NaF radiator.

Source: By the author

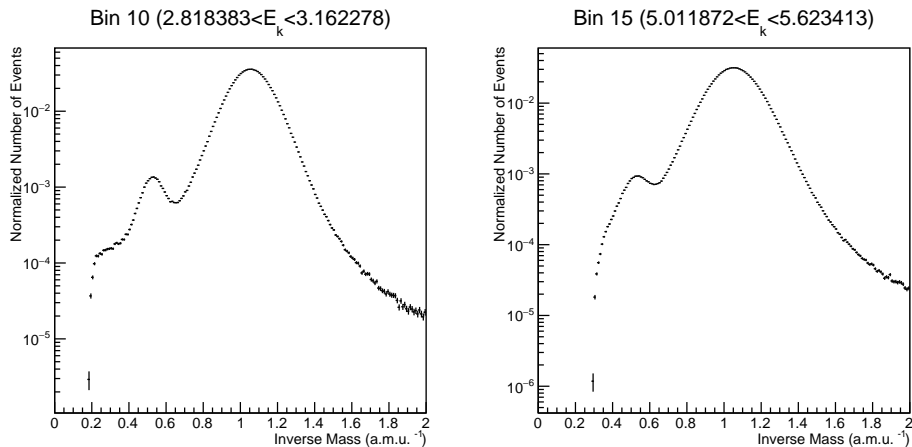


Figure 30 – The  $1/m$  distribution for two kinetic energy, measured in GeV/n, bins, for events whose velocity is measured by the aerogel radiator.

Source: By the author

The mass is computed by combining the rigidity and the velocity measurements. For this reason, the mass resolution depends both on the rigidity and  $\beta$  resolutions as follows:

$$\left(\frac{\Delta m}{m}\right)^2 = \left(\frac{\Delta R}{R}\right)^2 + \gamma^4 \left(\frac{\Delta \beta}{\beta}\right)^2 \quad (3.14)$$

The mass resolution for helium events is shown in Figure 31 for both data and simulated events detected by the AMS-02 experiment. The three regions correspond to the measurements of the velocity performed with the TOF, the RICH-NaF and the RICH-aerogel. At the low energy edge of each of the three regions, the mass resolution is dominated by the rigidity resolution, while at high energies the  $\beta$  resolution dominates.

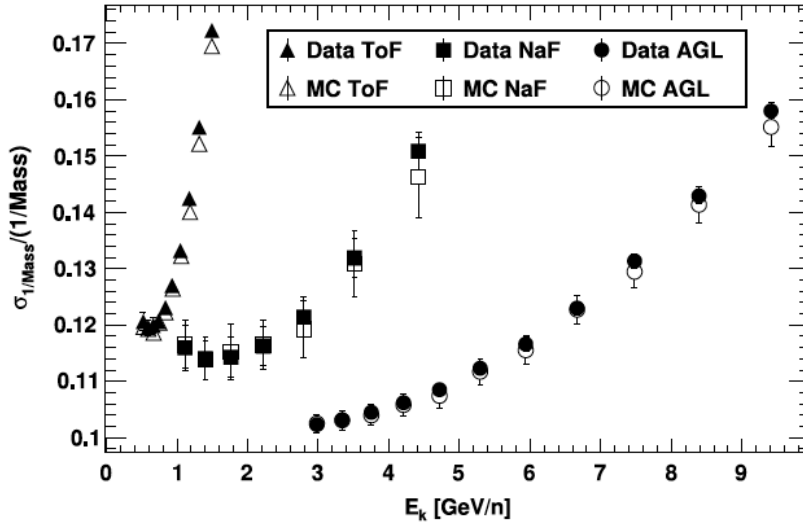


Figure 31 – The mass resolution  $1/m$  for data and simulations for helium events detected by the AMS-02 experiment. The data are shown as filled symbols and the MC simulation as open symbols. The triangles are from the TOF region, the squares indicate the RICH-NaF and the circles indicate the results for the aerogel.

Source: XIA et al.<sup>47</sup>

## 4 MEASUREMENT OF $^2\text{H}$ AND $^1\text{H}$ WITH THE AMS-02 DETECTOR

In this chapter we present the results of the measurement of the deuterium to hydrogen flux ratio between 0.7 to 7  $\text{GeV}/n$ , based on the data collected by the AMS-02 experiment between May 2011 and May 2014.

The AMS-02 experiment has an average trigger rate of about 700 Hz: out of the sample of triggered events we apply several selection criteria to identify well-reconstructed, single-charged down-going events. The key detectors used in this analysis are the tracker and the RICH: the former is used to measure the rigidity and the charge for each event, while the latter is used to measure the particle velocity.

There are three important sources of background affect the hydrogen and especially the deuterium identification in CRs. High charge nuclei can fragment inside the AMS detector and be incorrectly classified as deuterium or hydrogen events. Hydrogen nuclei being the most abundant component in CRs, the contribution of fragmented nuclei is not extremely relevant for the  $m \approx 1 \text{ GeV}/c^2$  region of measurement, however, the fragmentation can easily become an issue for the  $m \approx 2 \text{ GeV}/c^2$  region, as the expected deuterium fraction for the energy range considered is of the order of a few percent, such that a small number of fragmented events can contaminate the deuterium measurement. Hydrogen nuclei with poor mass reconstruction also affects the deuterium measurement. And finally helium nuclei, being the second most abundant component of the CRs, charge misidentification is particularly dangerous for deuterium identification, since a helium event misidentified as a single-charged event will have a mass measurement in the deuterium region.

Using simulated hydrogen and deuterium, as well as helium, events the first step of our analysis consisted in establishing a set of selection criteria aiming at minimizing the misidentified events while keeping a high statistics on the signal.

The selection criteria used in this analysis can be grouped into four categories, namely:

- **Pre-selection:** At this stage we apply basic selections to discard negative and multiple charged particles, particles coming from below the detector, events which have not triggered the data acquisition and events that pass through known bad detection channels.
- **Event quality selection:** Well reconstructed events are identified using the information collected by the silicon tracker, the TOF and the RICH. Events that have multiple tracks or particles are excluded, redundant measurements are checked for inconsistencies and poorly reconstructed events are discarded. In this category are also included selections that were good at rejecting events with bad mass reconstruction.

- **Helium rejection selection:** the first charge identification is mainly performed using the charge measured by the first layer of the tracker, located at the top of the instrument. Further selections are applied to exclude remaining misidentified or fragmented helium events.
- **Galactic CR selection:** this selection criterium aims to identify genuine CR events created in galactic sources while discarding particles produced by the interactions of CRs with the outer layers of the Earth's atmosphere. We require that the rigidity of each event exceed a critical rigidity, defined as 1.2 times the cutoff rigidity computed in the Stoermer approximation, as presented in 1.4.4.

The **pre-selection** consists of the following criteria:

- **ToF trigger:** the selected events must have triggered the data acquisition.
- **Tracker charge:** The charge measured by the tracker must be compatible with a single-charged particle,  $0.66 < Q_{TRK} < 1.55$ .
- **Relativistic events:** we set an initial constraint on  $\beta$  using the TOF measurement. Although the RICH measurement of  $\beta$  is more accurate, the TOF measurement can distinguish between up-going and down-going particles, and so this requirement eliminates up-going particles (likely to enter from the ECAL), whose properties would be misidentified. Namely, we require  $\beta_{TOF} > 0.3$ .
- **RICH quality cuts:** a few RICH radiator tiles are known to have some operational problems. The tile used for the detection of the particle is inferred by the particle's reconstructed track and stored in the data. Events passing through known bad tiles are excluded from the analysis.

The **quality selection** consists of the following criteria:

- **Single track events and single RICH ring:** these requirements are meant to help discard events with interaction or fragmentation inside the AMS-02 detector.
- **Tracker track reconstruction quality:** the tracker track  $\chi^2$  indicates the accuracy of the track reconstruction and is calculated independently for both the bending plane (Y) and non-bending plane (X). Single-charged particles track can be difficult to reconstruct due to noise signal effects in the silicon planes of the tracker and also to the presence of multiple particles due to particle fragmentation inside AMS. This cut rejects events which have a large uncertainty on the rigidity measurement. In particular, we require  $\chi^2 < 5(7)$  in the bending (non-bending) plane.

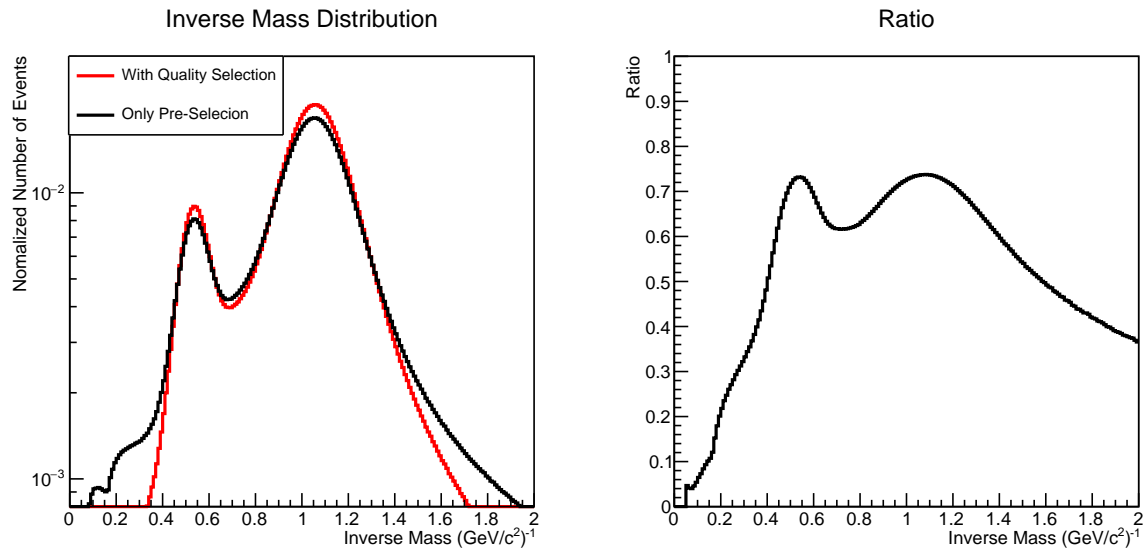


Figure 32 – On the left plot the distribution of the normalized inverse mass before and after the quality selection is applied is shown. The right plot shows the ratio of events after and before the applied selection.

Source: By the author

- **Detector Lifetime:** a cut on the lifetime of the detector, defined as the fraction of time during which the instrument is ready to detect and record an event is applied. We require the event lifetime to be greater than 0.6 to ensure reliable detection conditions. This cut also excludes events that were taken when the detector was crossing the South Atlantic Anomaly, a region where Earth’s magnetic field is lower than its surroundings. This anomaly causes a higher rate of cosmic-ray events in this region, that are normally not well measured since the detector is not able to handle the amount of events arriving at the same time, which in turn reduces the lifetime in this region.
- **Particle velocity consistency check:** we require that the velocity measured by the TOF and RICH agree within 5%.
- **RICH ring reconstruction quality:** There are some variables calculated by AMS algorithms to indicate the quality of the reconstructed ring in RICH. The ring is required to be good and clean and also to have a good quality parameter, the Kolmogorov probability that can be calculated providing the probability result of applying a Kolmogorov test to the distribution of charge along the ring. This quantity is almost uniformly distributed between 0 and 1 for rings correctly reconstructed, and peaks at 0 for incorrectly reconstructed ones. Only events with this parameter greater to 0.01 were used.
- **Number of collected photoelectrons:** The ratio between the total number of

photoelectrons collected by the RICH photomultipliers and the number of photoelectrons collected by PMTs crossed by charged particles is required to be greater than 0.4. Requiring this ratio to be high helps to ensure that the ring reconstructed is in fact formed by Cherenkov radiation, and not by particles interacting with the photomultipliers.

- **RICH ring reconstruction consistency check:** Two algorithms are available for the reconstruction of the ring in the RICH, and we require that both algorithms provide compatible results by taking into account only events whose  $\beta_{RICH}$  inconsistency is smaller than 0.01 for events passing through NaF and smaller than 0.005 for events passing through aerogel.
- **Tracker track within the fiducial volume of the radiator plane:** This geometric cut guarantees that the reconstructed particle trajectory passes within the acceptance of the radiator material.

Figure 32 shows the effect of the **quality selection** on a data sample, integrated in kinetic energy per nucleon: the left plot shows the normalized distribution of the inverse mass before (black line) and after the selection (red line).

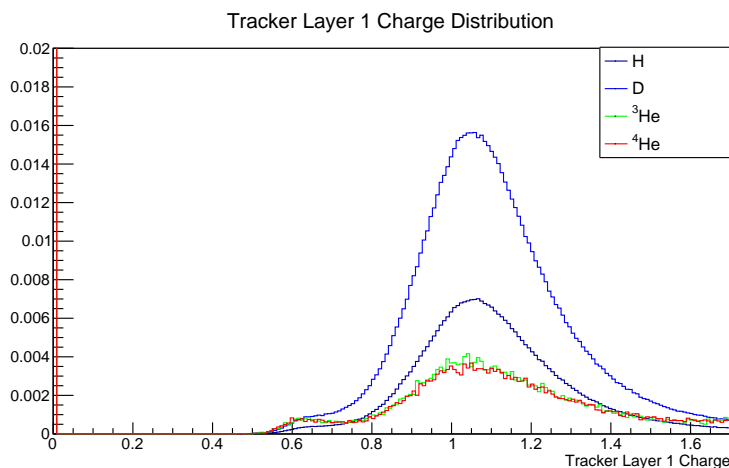


Figure 33 – Figure showing the charge measurement provided by the first tracker layer for simulated hydrogen, deuterium and helium reconstructed with charge one events. The graph is normalized, so that the curves represent the probability distribution function for that nucleus.

Source: By the author

The effect of these criteria is to reduce the number of events outside the hydrogen ( $1/m \approx 1 \text{ (GeV/c}^2\text{)}^{-1}$ ) and deuterium ( $1/m \approx 1/2 \text{ (GeV/c}^2\text{)}^{-1}$ ) regions. The right plot shows the ratio of the two distributions, non-normalized. It can be seen that the criteria provide good efficiency for the signal region while discarding many of the events outside it.

To reduce the contamination coming from misidentified helium events undergoing interactions inside the detector, we apply the following selection criteria:

- **Tracker layer one charge:** the first layer of the tracker provides the first measurement of the charge of the incoming particle. Since it is located on top of the detector, particles crossing it have not traversed much matter and thus had little chance to interact. Most helium events that will fragment either have a charge measurement around two or have not been detected in this layer. We select events whose charge is reconstructed by the first tracker layer, and its charge measurement is between 0.75 and 1.5, as motivated by the distributions in figure 33.
- **Inverse rigidity error estimate:** fragmented events may have a bad rigidity reconstruction, so the error on rigidity measurement helps to exclude helium events. We select events whose inverse rigidity error is between 0.85 and 1, as motivated by the distributions in figure 34.
- **Hits in the tracker:** few hits in the tracker might make poor charge and rigidity measurements, so this cut may help to exclude helium events. We select events with more than three hits in the tracker, motivated by the distributions in figure 35.
- **TOF charge:** We select events whose reconstructed TOF charge is between 0.8 and 1.1, as motivated by the distributions in figure 36.

After all selections, our sample is composed of  $\sim 50$  million events whose velocity is measured by the NaF and  $\sim 140$  million events whose velocity is measured by the aerogel.

The inverse mass distribution for the selected events as a function of kinetic energy per nucleon is shown in figure 37 and 38 for both NaF and aerogel.

It is possible to see the peaks for deuterium and hydrogen, NaF being able to discriminate these nuclei from about  $0.7 \text{ GeV}/n$  to around  $4 \text{ GeV}/n$ , after which the proton tail encompasses the deuterium peak. For aerogel events, this separation ranges from around  $2.5$  to  $7 \text{ GeV}/n$ .

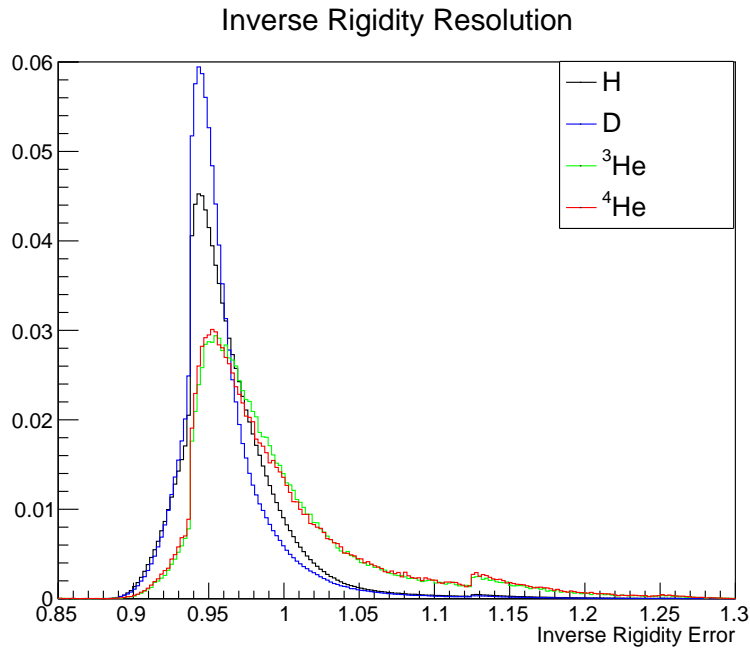


Figure 34 – Figure showing the error associated with the inverse rigidity measurement by the tracker for simulated hydrogen, deuterium and helium reconstructed with charge one events. The graph is normalized, so that the curves represent the probability distribution function for that nucleus.

Source: By the author

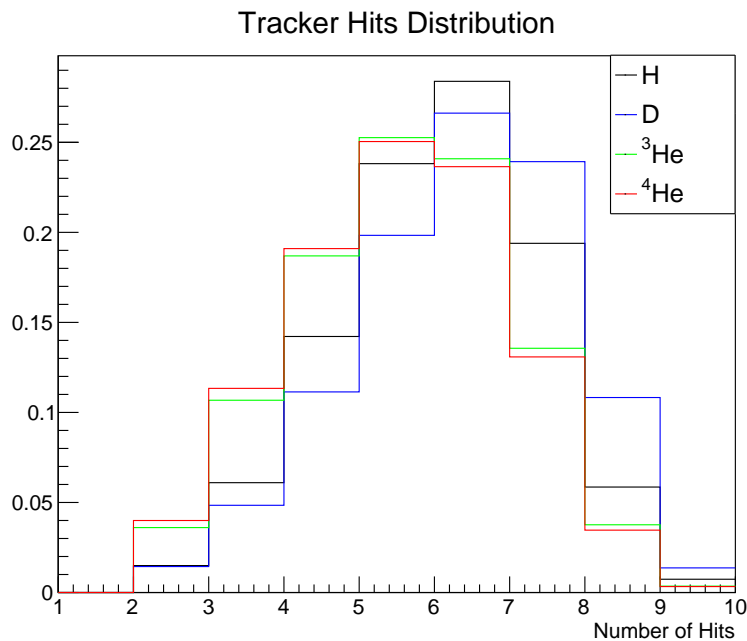


Figure 35 – Figure showing the number of hits in the tracker layers for simulated hydrogen, deuterium and helium reconstructed with charge one events. The graph is normalized, so that the curves represent the probability distribution function for that nucleus.

Source: By the author

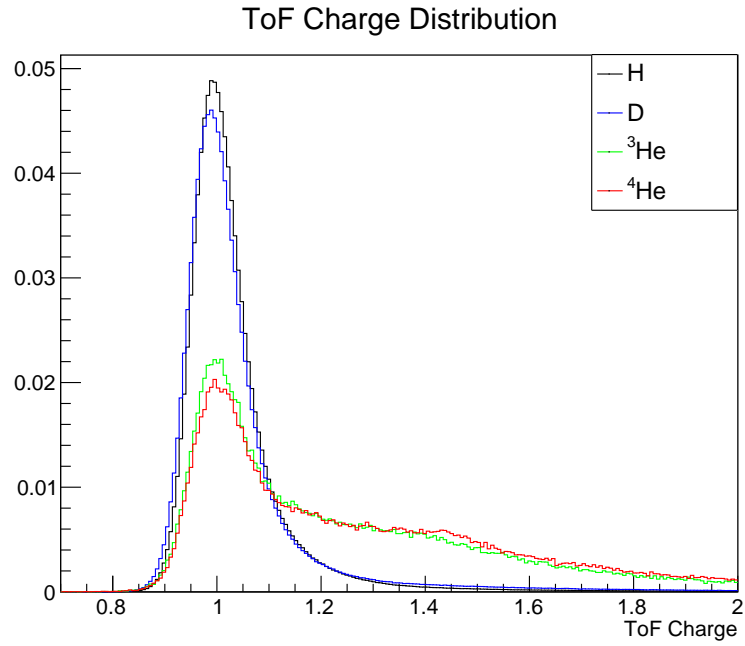


Figure 36 – Figure showing the charge measured by TOF for simulated hydrogen, deuterium and helium reconstructed with charge one events. The graph is normalized, so that the curves represent the probability distribution function for that nucleus.

Source: By the author

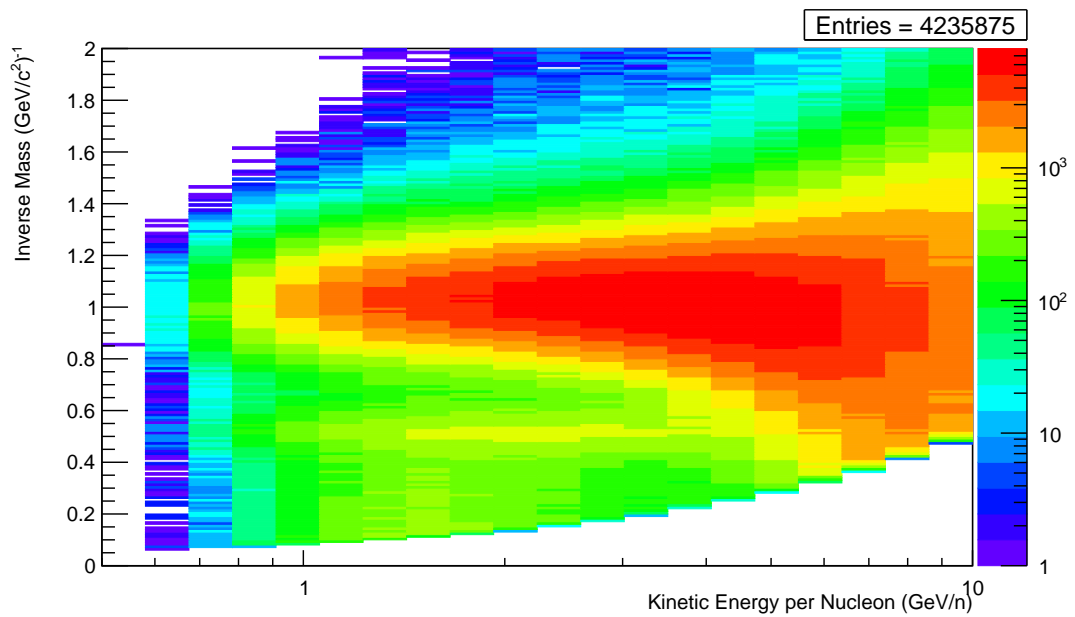


Figure 37 –  $1/m \times$  Kinetic Energy Profile for events whose velocity is measured with the NaF.

Source: By the author

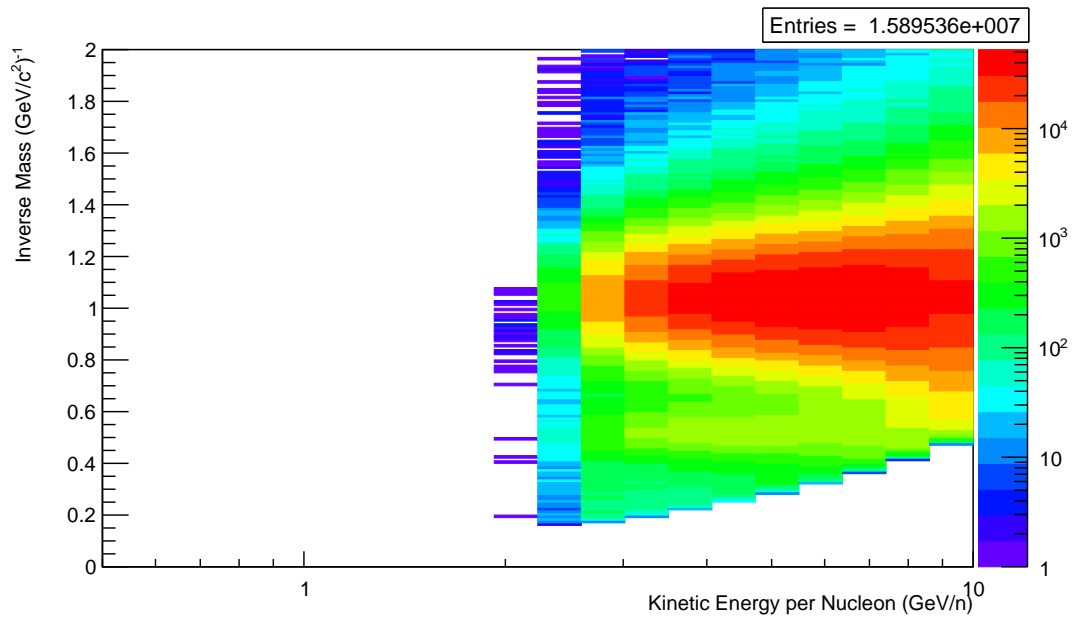


Figure 38 –  $1/m \times$  Kinetic Energy Profile for events whose velocity is measured with the aerogel.

Source: By the author

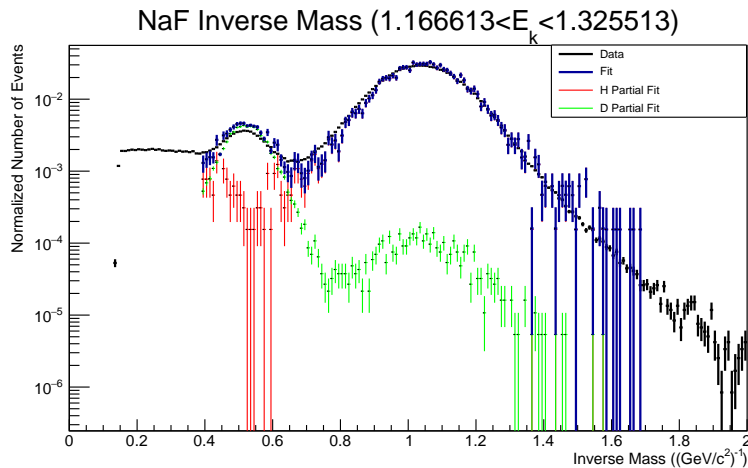


Figure 39 – Fit results for NaF events.

Source: By the author

#### 4.1 Event counting Method

The selection described in the previous section is applied to data, to identify the signal events over 18 bins in kinetic energy per nucleon between 0.5 to 7  $GeV/n$ . In each bin, the  $1/m$  reference spectra of the deuteron and hydrogen signal are used as templates. The templates are constructed from simulated events to which the same selection criteria described in the previous section are applied. A template for each bin is built.

Some of the fit results are shown in figures 39, for events whose velocity is reconstructed by the NaF, and 40, for events whose velocity is reconstructed by the Aerogel. For each plot, the data curve is shown in black, together with both fitted  $^2H$  and  $^1H$  templates, in green and red, respectively, and the total fit, that is, the sum of the fitted templates, in blue. The fit is performed in the inverse mass range between 0.4 and 1.7  $(GeV/c^2)^{-1}$ .

These fits count the number of deuterium and hydrogen detected, which must be further corrected to obtain the final  $^2H$  and  $^1H$  ratio. The number of events counted is summarized in table 1 for events whose velocity is reconstructed by the NaF and in table 2 by the Aerogel.

The error bars associated with MC templates are larger than the data error bars, this is due to the fact that given the limited time available to perform this work we only had access to a fraction of the simulated events, such that the statistical uncertainty is large, while the data sample is larger, implying smaller statistical uncertainty.

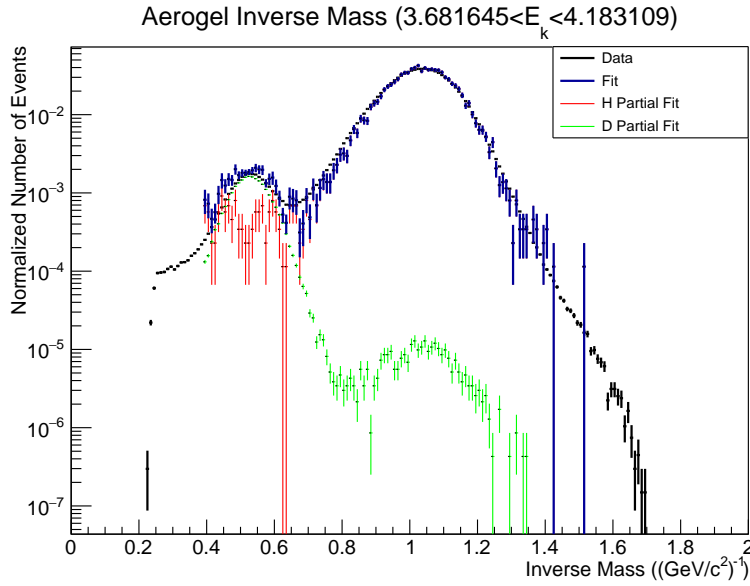


Figure 40 – Fit results for Aerogel events.

Source: By the author

Table 1 – Event count performed by NaF.

$E_k$ Range ( $GeV/n$ )	Number of Hydrogen	Number of Deuterium
0.700 - 0.765	131418	13136
0.765 - 0.904	332517	29256
0.904 - 1.03	582768	50021
1.03 - 1.17	842143	72290
1.17 - 1.33	1102824	85346
1.33 - 1.51	1346296	87397
1.51 - 1.71	1564303	93133
1.71 - 1.94	1777596	92391
1.94 - 2.21	1990948	88461
2.21 - 2.51	2185771	86649
2.51 - 2.85	2374552	86417
2.85 - 3.24	2596776	80224
3.24 - 3.68	2809895	73027

Source: By the author

## 4.2 Flux ratio measurement

The flux of a given CR particle can be expressed as:

$$\Phi(E_k) = \frac{N(E_k)}{Acc(E_k) \cdot \epsilon \cdot Exp(E_k) \cdot \Delta E_k} \quad (4.1)$$

where  $E_k$  is the kinetic energy per nucleon,  $N(E_k)$  is the number of signal events in the given bin,  $Acc(E_k)$  is the geometrical acceptance of the detector,  $\epsilon$  is the efficiency of the selection and  $\Delta E_k$  indicates the bin width. Assuming that hydrogen and deuterium events

Table 2 – Event count performed by Aerogel.

$E_k$ Range ( $GeV/n$ )	Number of Hydrogen	Number of Deuterium
2.85 - 3.24	1511708	77357
3.24 - 3.68	3857397	128211
3.68 - 4.18	6556083	158847
4.18 - 4.75	8955002	170190
4.75 - 5.40	10907262	162978
5.40 - 6.14	12250171	136011
6.14 - 7.00	12762840	132677

Source: By the author

have the same acceptance as well as the same exposure time as a function of kinetic energy per nucleon, the flux ratio can be simply obtained by the ratio of the number of events corrected by the efficiency ratio.

The particles passing the selection are classified as either hydrogen or deuterium nuclei. However, our data sample is contaminated by a small fraction of nuclei which are misidentified as single-charged events, especially because of fragmentation inside the detector. Since helium is the second most abundant component of CRs, a correction will be applied to the number of deuterium events in order to discard those misidentified events, while this effect is neglected for hydrogen nuclei, given their overabundance. The amount of helium can be estimated by applying the same selection used on the data sample to a helium MC sample, for each energy bin and radiator material.

Now we apply these corrections and provide an error estimation to the result.

- Selection Efficiency Correction:

The correction due to the selection efficiency is shown in figure 41 for events passing through NaF and Aerogel.

- Helium Contamination Correction:

The effect helium contamination has on the proton measurement is negligible, only its effect on deuterium measurement will be taken into account. To estimate this the amount of surviving helium and its effect on the deuterium fraction measurement is estimated. The amount of surviving helium can be estimated by applying the same selection used on the data sample to a helium MC sample, in the approximate helium-to-proton fraction expected for that energy region, for each energy bin and radiator material. This will give the amount of the surviving helium-to-proton ratio that will affect the measurement. To estimate its effect on the deuterium measurement we multiply it by the probability, based on the helium template, that the helium

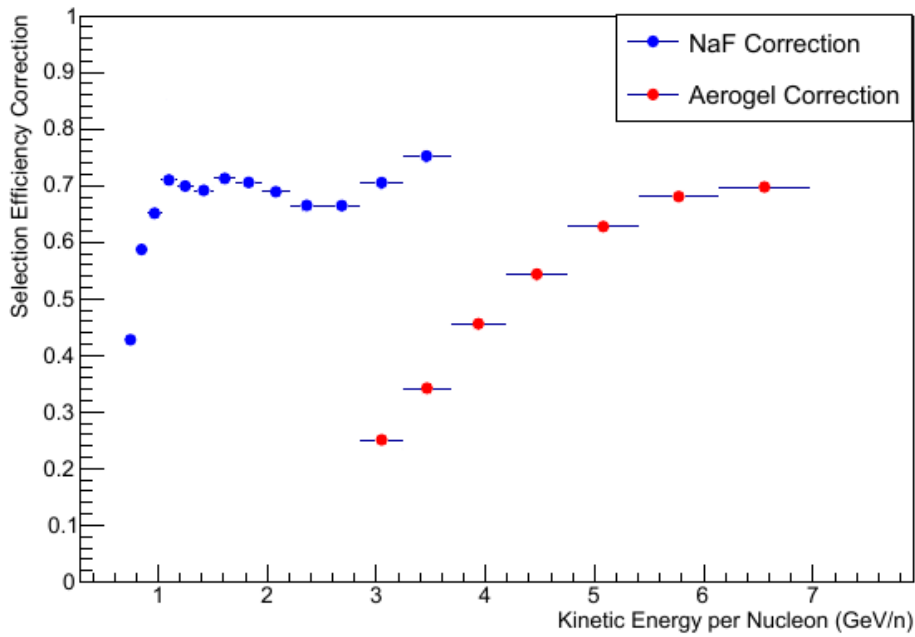


Figure 41 – Selection efficiency correction.

Source: By the author

inverse mass measurement will be in the deuterium region and thus contribute to the deuterium count. Figure 42 shows the calculated helium contamination correction.

- Statistical Error:

From the number of events counted, a statistical error can be estimated using the standard deviation associated with a Poisson distribution, that is, the error in the event count can be estimated as the square root of the number of counts. The relative statistical error obtained is shown in figure 43.

- Systematic error due to the event selection:

We can estimate the selection effect on the resulting deuterium fraction by slightly varying the section used and obtaining various deuterium fraction results, taking the standard deviation of the obtained results as the estimated error of the obtained deuterium fraction. The relative error is shown in figure 44.

### 4.3 Final Results

After applying the corrections and errors, a measurement of the number of arriving hydrogen and deuterium is made. The results are shown in tables 3 for events whose velocity is reconstructed by the NaF and 4 by the Aerogel.

This analysis is one of the first to be focused on hydrogen isotopic composition with AMS-02 data, and our results are in fair agreement with a similar and independent

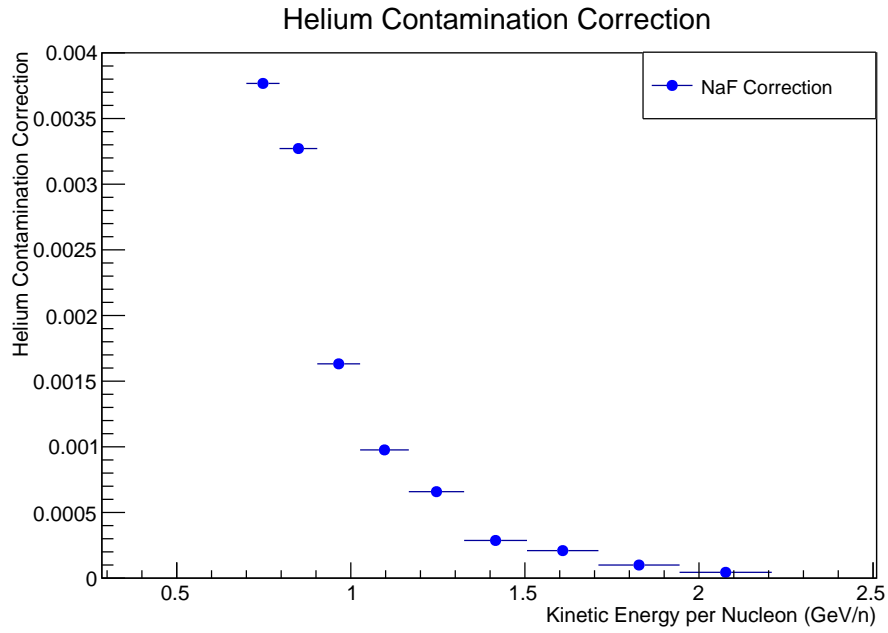


Figure 42 – Helium contamination correction.

Source: By the author

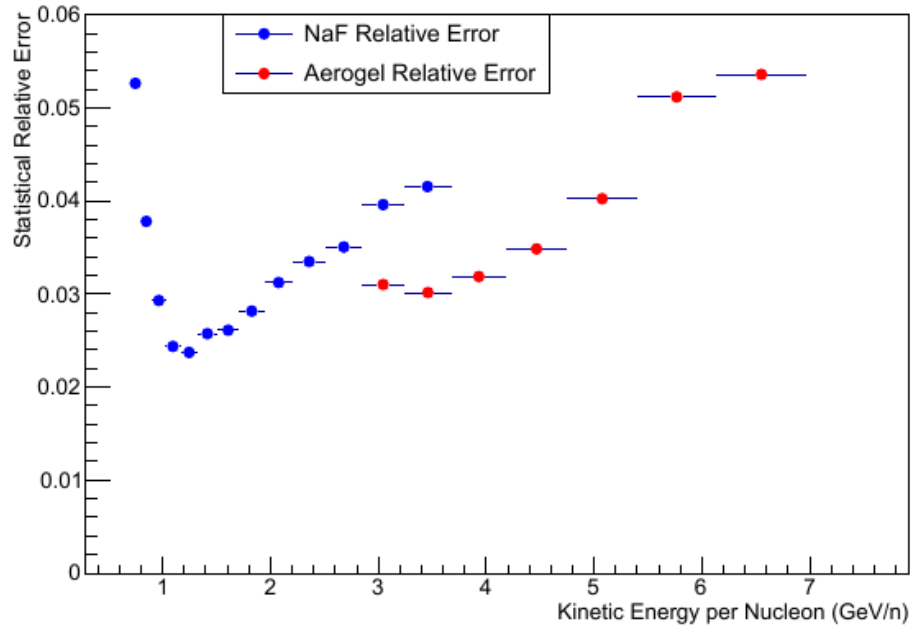


Figure 43 – Statistical relative error obtained.

Source: By the author

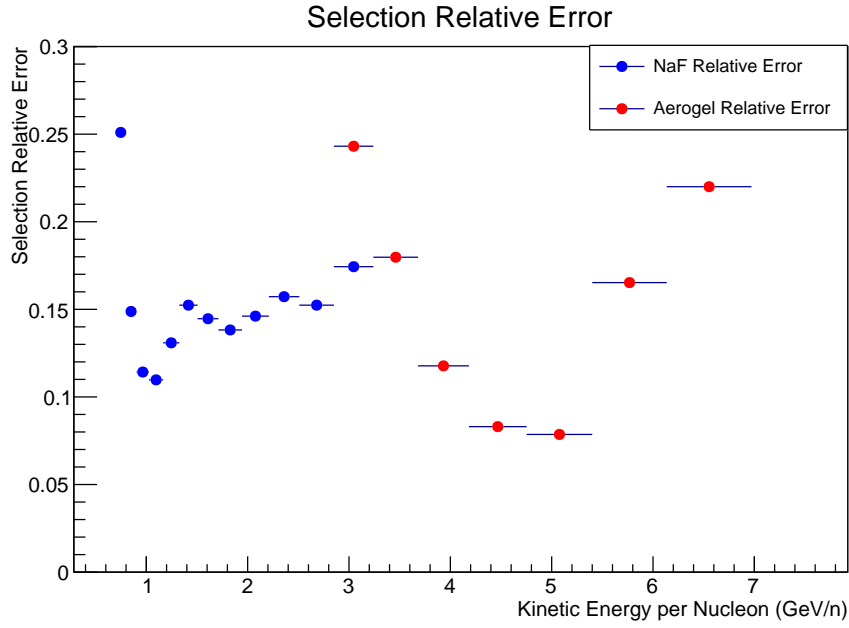


Figure 44 – Event selection systematic error.

Source: By the author

Table 3 – Corrected hydrogen and deuterium measurements performed by NaF.

$E_k$ Range ( $GeV/n$ )	Number of Hydrogen	Number of Deuterium
0.7 - 0.765	$1460195 \pm 258128$	$60136 \pm 10631$
0.765 - 0.904	$3358754 \pm 356250$	$173174 \pm 18368$
0.904 - 1.03	$5157239 \pm 444900$	$287731 \pm 24822$
1.03 - 1.17	$7136804 \pm 605578$	$430678 \pm 36544$
1.17 - 1.33	$9190199 \pm 1039752$	$497141 \pm 56245$
1.33 - 1.51	$10684888 \pm 1163525$	$479990 \pm 52268$
1.51 - 1.71	$12317343 \pm 1228064$	$519200 \pm 51765$
1.71 - 1.94	$13569437 \pm 1324116$	$494396 \pm 48244$
1.94 - 2.21	$15554281 \pm 1572791$	$486536 \pm 49197$
2.21 - 2.51	$17347392 \pm 1938100$	$484132 \pm 54089$
2.51 - 2.85	$19463539 \pm 2078183$	$496545 \pm 53018$
2.85 - 3.24	$21821651 \pm 2731152$	$508307 \pm 63619$
3.24 - 3.68	$25314373 \pm 3204094$	$271054 \pm 34308$

Source: By the author

analysis that has been carried out within the Collaboration. The obtained flux ratio is still being worked upon within the Collaboration.

Table 4 – Corrected hydrogen and deuterium measurements performed by Aerogel.

$E_k$ Range ( $GeV/n$ )	Number of Hydrogen	Number of Deuterium
2.85 - 3.24	$15269781 \pm 2591368$	$189094 \pm 32090$
3.24 - 3.68	$32689805 \pm 4091387$	$369422 \pm 46236$
3.68 - 4.18	$51622703 \pm 4124812$	$554087 \pm 44273$
4.18 - 4.75	$68358795 \pm 3963631$	$701546 \pm 40678$
4.75 - 5.40	$81397474 \pm 4546980$	$756512 \pm 42260$
5.40 - 6.14	$88769354 \pm 10105875$	$670200 \pm 76298$
6.14 - 7.00	$95961200 \pm 14520930$	$696307 \pm 105366$

Source: By the author



## 5 CONCLUSIONS AND PERSPECTIVES

The measurement of the composition and spectra of cosmic rays provides crucial information regarding CR sources, their acceleration and propagation mechanisms. The  $^2\text{H}/^1\text{H}$  flux ratio between 0.7 and 7 GeV/n have been performed using the data collected by the AMS-02 experiment between May 2011 and May 2014.

The obtained results extend the measurement range of previous experiments and points to the expected decay in the deuterium ratio in the energy region considered, supporting both the standard models of CRs propagation, that of deuterium being purely a secondary particle in CRs, and the model where it would be produced inside certain types of star.<sup>25</sup> To exclude one of these scenarios the energy range of the analysis must be further extended. This may be able to be done by achieving a better mass reconstruction.

The work done can be further developed. The main difficulties of this study are the background presence of both helium events, present in great quantities in CRs compared to the desired deuterium measurement, and proton events with bad mass reconstruction, driven by the error in the velocity measurement performed by RICH. So the main goals of further efforts in this analysis should be to achieve a higher helium rejection capability and a more precise velocity measurement. The work can also be expanded in a few ways. Some suggestions are discussed below.

- Expand the number of variables used to choose selections, as well as use more complex selection techniques - such as using multi-dimensional plots to look for the presence of clusters of unwanted events that are difficult to see with the single variable analysis used for this work. Machine learning algorithms can be very useful for this purpose.
- Correct for energy losses in the detector. Every measurement made by the AMS detector takes some energy of the particle, altering its momentum and velocity. Since we are dealing with heavy particles and the RICH subdetector is one of the last subdetectors in AMS the velocity alteration is more important. The measure of energy deposited in various subdetectors of AMS can help to reconstruct a more precise velocity.
- Use, in addition to proton and deuterium templates, a helium template to fit the data curve as a sum of proton, deuterium and helium. The initial difficulty for this is that helium has peaks in both the  $m \approx 1$  and  $m \approx 2$  regions, so that without information on the quantity of helium to be used the inverse mass distribution can be reasonably well described with only protons and helium. To solve this problem

the amount of helium must be supplied, either by an estimation from the known He/H fraction or by the measurement of the helium flux along with the proton and deuterium ones.

- Due to the large amount of data available the time dependence of the  $^2\text{H}/^1\text{H}$  fraction can be measured, searching for correlation with transient phenomena related with the activity of the Sun.

## REFERENCES

- 1 LONGAIR, M. S. **High energy astrophysics**. 3rd ed. Cambridge: Cambridge University Press, 2011. 880 p.
- 2 PATRIGNANI, K. e. a. Review of particle physics. **Chinese Physics C**, v. 38, n. 9, p. 090001, 2014.
- 3 AHARONIAN, F.; BERGSTRÖM, L.; DERMER, C. **Astrophysics at very high energies**, 2013. Berlin: Springer, 2013. (Saas-Fee advanced course, 40).
- 4 UCHIYAMA, Y. et al. **Fermi-LAT Discovery of GeV Gamma-ray Emission from the Vicinity of SNR W44**. Available from: <<http://arxiv.org/pdf/1203.3234.pdf>>. Accessible at: 17 Aug. 2017.
- 5 ANGELIS, A. D.; PIMENTA, M. M. **Introduction to particle and astroparticle physics: questions to the universe**. Milan: Springer, 2015.
- 6 BEREZINSKY, V. S.; GAZIZOV, A.; GRIGORIEVA, S. On astrophysical solution to ultrahigh energy cosmic rays. **Physical Review D**, v. 74, 2006.
- 7 BEREZINSKY, V. S.; GRIGORIEVA, S. A bump in the ultra-high energy cosmic ray spectrum. **Astronomy & Astrophysics**, v. 199, p. 1–12, 1988. ISSN: 0004-6361).
- 8 BLANDFORD, R. Acceleration of ultra high energy cosmic rays. **Physica Scripta**, v. T85, p. 191–194, 2000.
- 9 WATSON, A. A. High-energy cosmic rays and the greisen–zatspepin–kuz'min effect. **Reports on Progress in Physics**, v. 77, n. 3, p. 036901, 2014.
- 10 ABRAHAM, J. et al. Observation of the suppression of the flux of cosmic rays above  $4 \times 10^{19}$  eV. **Physical Review Letters**, v. 101, p. 061101, Aug 2008.
- 11 MELLO NETO, J. **Ultra high energy cosmic rays: the highest energy frontier**. 2015. Available from: <<https://arxiv.org/pdf/1510.05629.pdf>>. Accessible at: 17 Aug. 2017.
- 12 SIMPSON, J. A. Elemental and isotopic composition of the galactic cosmic rays. **Annual Review of Nuclear and Particle Science**, v. 33, n. 1, p. 323–382, 1983. Available from: <<http://authors.library.caltech.edu/45081/1/1982-05.pdf>>. Accessible at: 17 Aug. 2017.
- 13 BOUDAUD, M. et al. **A new look at the cosmic ray positron fraction**. 2015. Available from: <[https://pos.sissa.it/archive/conferences/236/1183/ICRC2015\\_1183.pdf](https://pos.sissa.it/archive/conferences/236/1183/ICRC2015_1183.pdf)>. Accessible at: 17 Aug. 2017.
- 14 CUOCO, A.; KRÄMER, M.; KORSMEIER, M. Novel dark Matter constraints from antiprotons in light of AMS-02. **Physical Review Letters**, v. 118, n. 19, p. 191102, 2017.
- 15 SAEKI, T. et al. A new limit on the flux of cosmic anti-helium. **Physics Letters B**, v. 422, n. 1-4, p. 319–324, 1998.

16 BELOTSKY, K. et al. Anti-helium flux as a signature for antimatter globular clusters in our Galaxy. **Physics of Atomic Nuclei**, v. 63, n. 2, p. 233–239, 2000.

17 VEREECKEN, M. **Cosmic ray shock acceleration in galactic and extragalactic sources**. 2014. Ph. D. Thesis, 2014. Available from: <[http://lib.ugent.be/fulltxt/RUG01/002/163/589/RUG01-002163589\\_2014\\_0001\\_AC.pdf](http://lib.ugent.be/fulltxt/RUG01/002/163/589/RUG01-002163589_2014_0001_AC.pdf)>. Accessible at: 17 Aug. 2017.

18 SOKOLOV, I. V. et al. Diffusive shock acceleration theory revisited. **Astrophysical Journal**, v. 642, n. 1, p. 81–84, 2006.

19 MELROSE, D. B. **Acceleration mechanisms**. 2009. Available from: <<https://arxiv.org/pdf/0902.1803.pdf>>. Accessible at: 17 Aug. 2017.

20 GRENIER, I. A.; BLACK, J. H.; STRONG, A. W. The nine lives of cosmic rays in galaxies. **Annual Review of Astronomy and Astrophysics**, v. 53, p. 199–246, 2015. Available from: <<http://www.annualreviews.org/doi/pdf/10.1146/annurev-astro-082214-122457>>. Accessible at: 17 Aug. 2017.

21 STRONG, A. W.; MOSKALENKO, I. V.; PTUSKIN, V. S. Cosmic-ray propagation and interactions in the galaxy. **Annual Review of Nuclear and Particle Science**, v. 57, n. 1, p. 285–327, 2007.

22 GENOLINI, Y. et al. **Indications for a high-rigidity break in the cosmic-ray diffusion coefficient**. 2017. Available from: <<https://arxiv.org/pdf/1706.09812.pdf>>. Accessible at: 17 Aug. 2017.

23 PUTZE, A.; DEROME, L.; MAURIN, D. **A Markov Chain Monte Carlo technique to sample transport and source parameters of galactic cosmic rays II. results for the diffusion model combining b / c and radioactive nuclei**. Available from: <<https://arxiv.org/pdf/1001.0551.pdf>>. Accessible at: 17 Aug. 2017.

24 VUKCEVIC, M. **Solar activity synchronization modulation**. . Available from: <<http://www.vukcevic.talktalk.net/LFC5.htm>>. Accessible at: 17 Aug. 2017.

25 TOMASSETTI, N. et al. The curious case of high-energy deuterons in Galactic cosmic rays. **Astrophysical Journal**, v. 835, n. 2, p. L26, 2017.

26 MAURIN, D. et al. A database of charged cosmic rays. **Astronomy & Astrophysics**, v. 569, p. A32, 2014. Available from: <<https://arxiv.org/pdf/1302.5525.pdf>>. Accessible at: 17 Aug. 2017.

27 BEATTY, J. J. et al. The cosmic-ray he-3/he-4 ratio from 100 to 1600 MeV/amu. **Astrophysical Journal**, v. 413, p. 268, 1993. doi: 10.1086/172994.

28 AGUILAR, M. et al. Relative composition and energy spectra of light nuclei in cosmic rays. results from ams-01. **Astrophysical Journal**, 2010. Available from: <<http://arxiv.org/abs/1008.5051>>. Accessible at: 17 Aug. 2017.

29 TURUNDAEVSKIY, A.; PODOROZHNYI, D. High energy deuterons in cosmic rays registered by the SOKOL satellite experiment. **Advances in Space Research**, v. 59, n. 1, p. 496–501, 2017.

- 
- 30 TING, S. The alpha magnetic spectrometer on the international space station. **International Journal of Modern Physics E**, v. 21, n. 08, p. 1230005, Aug. 2012.
- 31 AGUILAR, M. et al. First result from the alpha magnetic spectrometer on the international space station: Precision measurement of the positron fraction in primary cosmic rays of 0.5–350 gev. **Physical Review Letters**, v. 110, n. 14, p. 141102, 2013.
- 32 KIRN, T. The ams-02 trd on the international space station. **Nuclear Instruments and Methods in Physics Research Section A**, v. 706, n. 1, p. 43 – 47, 2013. Doi:10.1016/j.nima.2012.05.010.
- 33 DOETINCHEM, P. V. et al. Performance of the ams-02 transition radiation detector. **Nuclear Instruments and Methods in Physics Research, Section A**, v. 558, n. 2, p. 526–535, 2006.
- 34 BINDI, V. et al. Calibration and performance of the ams-02 time of flight detector in space. **Nuclear Instruments and Methods in Physics Research Section A**, v. 743, n. 1, p. 22 – 29, 2014.
- 35 VAGELLI, V. **Identification of positrons and electrons in the cosmic radiation with the electromagnetic calorimeter ECAL for the AMS-02 experiment**. 2011. 90 p. Dissertation (Master) — Facolt'a di Scienze Matematiche Fisiche e Naturali, Universit'a di Pisa, Pisa, 2011.
- 36 ALCARAZ, J. et al. Erratum to: “the alpha magnetic spectrometer silicon tracker: Performance results with protons and helium nuclei” [nucl. instr. and meth. a 593 (2008) 376–398]. **Nuclear Instruments and Methods in Physics Research Section A**, v. 597, n. 2, p. 270, 2008.
- 37 AMBROSI, G. et al. The spatial resolution of the silicon tracker of the Alpha magnetic spectrometer. **Nuclear Instruments and Methods in Physics Research Section A**, v. 869, n. 1, p. 29–37, 2017.
- 38 DURANTI, M. **Measurement of the atmospheric muon flux on ground with the AMS-02 detector**. 2011. 153 f. Ph. D. Thesis. (Physics) - Università degli Studi di Perugia, Perugia, 2011.
- 39 GILLARD, W. High precision measurement of the ams-rich aerogel refractive index with cosmic ray. In: INTERNATIONAL COSMIC RAY CONFERENCE (ICRC2013), 33., 2013, Rio de Janeiro. **Proceedings...** Rio de Janeiro: ICRC, 2013.
- 40 AMS-02. **The RICH**. 2017. Available from: <<http://www.ams02.org/what-is-ams/tecnology/rich/>>. Accessible at: 14 Aug. 2017.
- 41 DOETINCHEM, P. von et al. The ams-02 anticoincidence counter. **Nuclear Physics B - proceedings supplements**, v. 197, n. 1, p. 15 – 18, 2009.
- 42 ADLOFF, C. et al. The AMS-02 lead-scintillating fibres Electromagnetic Calorimeter. **Nuclear Instruments and Methods in Physics Research Section A**, v. 714, p. 147–154, 2013. doi:10.1016/j.nima.2013.02.020.
- 43 LEO, W. R. **Techniques for nuclear and particle physics experiments**. 2nd ed. Heidelberg: Springer-Verlag Berlin Heidelberg, 1994.

- 44 TOMASSETTI, N. et al. Identification of light cosmic-ray nuclei with ams-02. In: INTERNATIONAL COSMIC RAY CONFERENCE (ICRC2013), 33., 2013, Rio de Janeiro. **Proceedings...** Rio de Janeiro: ICRC, 2013.
- 45 ALPAT, B. et al. Charge determination of nuclei with the AMS-02 silicon tracker. **Nuclear Instruments and Methods in Physics Research Section A**, v. 540, n. 1, p. 121–130, 2005.
- 46 BERDUGO, J. et al. Determination of the rigidity scale of the Alpha Magnetic Spectrometer. **Nuclear Instruments and Methods in Physics Research Section A**, v. 869, n. 1, p. 10–14, 2017.
- 47 XIA, X. et al. Mass resolution for helium isotopes in AMS-02. **Nuclear Instruments and Methods in Physics Research Section A**, v. 868, n. 1, p. 139–141, 2017.